CHEMISTRY OF MATERIALS

Editors' Choice
Open Access

pubs.acs.org/cm

Article

Halometallurgy: Reduction of Battery Cathode Materials under a Quasi-Inert Environment of Alkali Chloride Salts

Arseniy Bokov,* Anna Shelyug, Liuda Mereacre, Michael Knapp, and Helmut Ehrenberg

Cite This: https://doi.org/10.1021/acs.chemmater.5c02896

Read Online

ACCESS | Metrics & More | Article Recommendations | Supporting Information

ABSTRACT: This study introduces halometallurgy, an approach for reducing common Li-ion cathode materials in air using a eutectic mixture of chloride salts, with direct implications for processing battery black mass containing NMC, NCA, LCO, LNMO, and LMO. In-depth analysis, including in situ XRD, SEM/EDX, and TGA-DSC, reveals that reduction in the presence of NaCl-KCl proceeds via distinct halothermal and carbothermal routes. During the halothermal stage, lithium migrates from cathode particles into the chlorides, leading to the decomposition of layered or spinel structures into a solid solution of cubic oxides. Lithium migration facilitates the melting of the salts, resulting in the encapsulation of the oxide phase and the creation of quasi-inert conditions. This enables further reduction during the carbothermal stage and promotes the nucleation of metallic crystallites. Upon washing with water, lithium predominantly remains in the saline solution, termed halothermal brine, while the insoluble fraction consists of porous transition metal oxides and graphite. Depending on cathode composition, halothermal reduction is observed at 460−640 °C, while carbothermal reduction occurs above 620−650 °C. Typical black-mass impurities, including current collectors, binders, and electrolyte residues, were also examined, demonstrating relevance for real waste streams. The proposed treatment offers a pathway toward decentralized battery recycling.

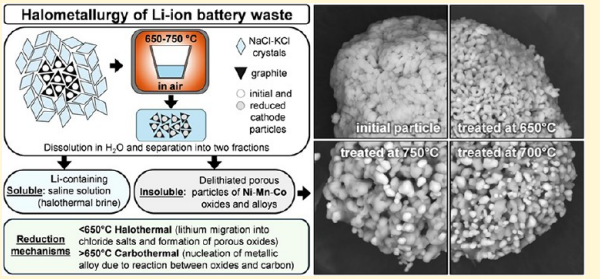

1. INTRODUCTION

The increased use of electric vehicles in recent decades has led to the accumulation of large quantities of spent lithium-ion cells, which can be considered a new source of critical raw materials.[1−3] Among the most suitable batteries for recycling are typically those with a high content of Ni, Mn, and Co in the cathode.[4] These include the polymetallic NCM or NMC type compositions, represented by the general formula $LiNi_xMn_yCo_zO_2$,[5] as well as $LiNi_xCo_yAl_zO_2$, commonly known as NCA,[6] and $LiNi_xMn_{2-x}O_4$ abbreviated as LNMO.[7] In addition, compounds based on a single transition metal, such as $LiCoO_2$,[8] $LiNiO_2$,[9] and $LiMn_2O_4$,[10] which are often found in older cells, are also suitable for the recovery of transition metals and lithium.

The conventional approach to handling Li-ion battery waste includes the collection of discarded packs and modules, followed by discharging, dismantling, and cell extraction.[11] The recovered cells are then shredded and sieved to remove coarse fragments of Al and Cu current collectors, as well as plastic pieces originating from the casing and separator.[12] The finest fraction from sieving is a black powder, commonly referred to as black mass, which primarily consists of cathode particles and graphite.[13] At the industrial scale, battery black mass is often processed via a hydrometallurgical route,[14] in which concentrated acids are used to convert the cathode materials into soluble transition metal salts, followed by the precipitation of lithium compounds. Other forms of waste, such as micro-batteries or damaged cells, can be directly subjected to a pyrometallurgical route,[15] where smelting at high temperatures enables the recovery of nickel and cobalt, while lithium is typically lost through evaporation or dissolution in the slag.

At the current level of technological development, hydrometallurgy is often viewed as a more efficient approach, since all elements can be extracted from spent batteries.[16] Despite its advantages, scaling of the existing facilities or construction of new plants requires high expenditures associated with managing and treating large volumes of acidic waste.[17,18] This issue could be mitigated by using reduced black mass, consisting of decomposed cathode materials.[19,20] Such powder is more amenable to the leaching of transition metals, as lower acid concentrations or less toxic reagents can be used.[21,22] However, the reduction process generally requires an inert environment, such as nitrogen,[23] argon,[24] or vacuum,[25] which imposes strict requirements on heating equipment and increases the overall cost of waste treatment.

Received: October 29, 2025
Revised: February 4, 2026
Accepted: February 6, 2026

The hypothesis of this study is that the reduction of battery cathode materials can be performed under air by relying on chloride salts, which create a quasi-inert environment. Recently, a salt-shielded approach was proposed for the synthesis of MAX phases.[26,27] These ordered crystal structures typically form only at high temperatures and under an inert atmosphere, where metals react directly with carbon.[28] Since a similar reaction is expected during the reduction of black mass, the use of salts might also be feasible for the treatment of battery waste.

Throughout the study, this hypothesis is examined using various analytical techniques, and the practical implications of the process are evaluated across different cathode materials and typical impurities. The results demonstrate that the interaction between cathode particles and alkali chloride salts proceeds through two distinct stages of reduction, halothermal and carbothermal, which provide the scientific basis for a battery recycling approach termed halometallurgy.

2. MATERIALS AND METHODS

The starting materials for this study were obtained as follows. The NaCl and KCl salts with 99% purity were received from Alfa Aesar (Thermo Scientific Chemicals). The synthetic graphite of KS-6L grade was sourced from C-NERGY. The cathode powders were purchased from various suppliers: $LiNi_{0.33}Mn_{0.33}Co_{0.33}O_2$ (BASF SE), $LiNi_{0.6}Mn_{0.2}Co_{0.2}O_2$ (BASF SE), $LiNi_{0.80}Co_{0.15}Al_{0.05}O_2$ (NEI Corporation), $LiCoO_2$ (Targray), $LiNi_{0.5}Mn_{1.5}O_4$ (Sigma-Aldrich), $LiMn_2O_4$ (Sigma-Aldrich), and $LiFePO_4$ (Sigma-Aldrich).

For simplicity and consistency with common notation in the literature, graphite and the other materials are hereinafter referred to as Gr, NMC (equimolar), NMC622, NCA, LCO, LMNO, LMO, and LFP, respectively. Additional reagents, such as Al, Cu, PVDF, and LiF, which were used to understand the effect of black-mass impurities, were also provided by the companies listed above. All starting materials were confirmed to be single phase (see Figure S1 in the Supporting Information).

Two sets of samples were prepared in parallel for ex situ and in situ experiments, using a mixture of 50.5 mol % NaCl and 49.5 mol % KCl, preannealed at 700 °C for 1 h to ensure formation of the eutectic. For the ex situ case, NMC particles were mixed with 40 wt % graphite and compacted into 10 mm disk-shaped pellets under 250 MPa pressure. Each pellet weighed about 0.25 g, with 0.18 g contribution from the cathode material and 0.07 g from the graphite. The compacted pellets were placed in 15 mL alumina crucibles, containing 0.9 g of NaCl-KCl, and then covered with extra 1.6 g of the same salt mix to achieve a 1:10 pellet-to-salt mass ratio.

For the in situ case, NMC with 40 wt % graphite was mixed with NaCl-KCl in a 1:1 mass ratio and loaded into 0.5 mm quartz capillaries of 80 mm length. Several reference experiments were also performed without cathode powder and/or without graphite. Similar in situ samples with graphite flakes and chloride salts were prepared using NMC622, NCA, LCO, LNMO, LMO, LiCl, Al, Cu, PVDF, and LiF to analyze the reduction process in the context of real battery waste.

The graphite content in the ex situ and in situ samples was set to 40 wt % with respect to the cathode powders, so that the resulting model mixtures resembled the composition of industrially produced black mass.[29] The same reasoning was used when selecting other materials to study the behavior of different cathode compositions and common impurities.[30−32] The amount of chloride salts relative to NMC-Gr was selected so that lithium constituted about 1 wt % of the total alkali content.

The heat treatment of the ex situ samples was performed in a Nabertherm L-3-11-C450 box furnace. The alumina crucibles, containing the NMC-Gr pellets and eutectic NaCl-KCl salts, were heated at a rate of 5 °C/min to 590−750 °C, followed by a 10 min dwell at the maximum temperature. Upon cooling, the samples were dissolved in deionized water, and the saline solution was separated from the insoluble part by centrifugation. The remaining powders were then washed three more times to facilitate further analysis.

The in situ samples were heated in a STOE capillary furnace (Figure S2), which consisted of a water-cooled stainless steel casing and a cylindrical heating element located at the center. During heating, nitrogen gas was flushed through the furnace to protect the graphite heater, while the upper part of the quartz capillary was exposed to ambient air. Heating was performed at a rate of 5 °C/min to 750 °C with pauses every 10 °C for data acquisition.

The structural evolution and the phase composition of the in situ and ex situ samples were analyzed by X-ray Diffraction (XRD) using a STOE STADI-P double-sided setup with the Mo−Kα_1 radiation (0.70932 Å), Ge(111) monochromator, and linear MYTHEN2 detector. The XRD scans for in situ samples were performed every 10 °C increment of the temperature profile, with each scan lasting 10 min. The detector operated in stationary mode centered at 15.9°, covering a 2θ range approximately from 7° to 25°.

The XRD analysis for the ex situ samples was performed using the same Mo wavelength, monochromator, and detector, but in a wider 2θ range of 5−45° with an angular resolution of 0.015° and total exposure time of 60 min. Prior to scanning, powdered samples were placed between round adhesive Kapton foils and mounted in a STOE transmission sample holder.

The morphology and elemental distribution maps of the ex situ samples were determined by Scanning Electron Microscopy (SEM) and Energy-Dispersive X-ray Spectroscopy (EDX) on a Zeiss FE-SEM Merlin. Prior to imaging, the samples were placed on carbon paper and mounted on aluminum pins. For image acquisition, a backscattered electron detector was used, with a working distance of 10 mm, an accelerating voltage of 15 kV, and a probe current of 10 nA. The imaging of the interfacial areas between NMC-Gr pellet and NaCl-KCl was performed after cleaving the samples.

The heat effects associated with transformations in the cathode material and chloride salts were analyzed using combined Thermogravimetric Analysis and Differential Scanning Calorimetry (TGA-DSC) with a Netzsch STA 449. The eutectic NaCl-KCl was mixed with NMC-Gr in various proportions and compacted into 3 mm pellets. The prepared pellets were placed in 85-μL alumina crucibles and heated to 700 °C at a rate of 10 °C/min under argon with 20 vol % of oxygen. Upon reaching the maximum temperature, the cooling profiles were recorded at the same rate. Additionally, selected samples were further characterized by optical microscopy and ICP-OES. Details of these techniques and the corresponding results are provided in the Supporting Information.

3. RESULTS AND DISCUSSION

The study began by testing the hypothesis that chloride salts could provide quasi-inert conditions for the reduction of

https://doi.org/10.1021/acs.chemmater.5c02896
Chem. Mater. XXXX, XXX, XXX−XXX

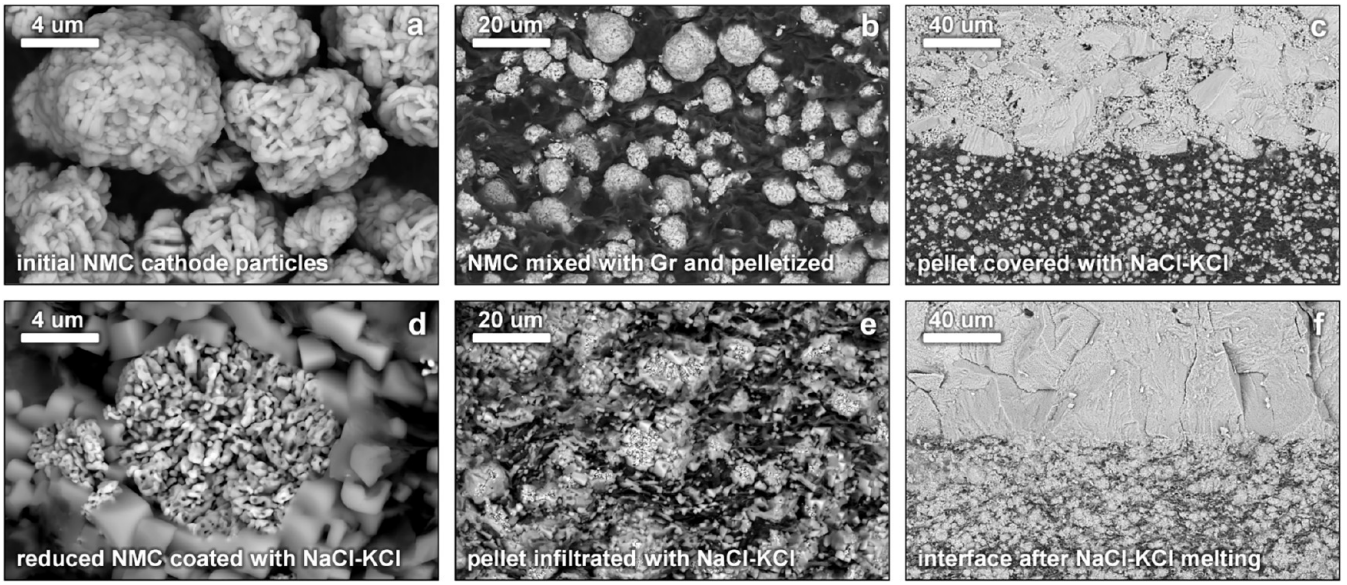

Figure 1. SEM images of NMC samples before (a-c) and after (d-f) heating to 670 °C with Gr and NaCl-KCl. Images are arranged for side-by-side comparison at the same magnification between (a,d), (b,e), and (c,f) to highlight changes in particle morphology, pellet microstructure, and the interfacial region.

cathode materials. To examine this, the common battery compound NMC was analyzed by SEM before and after the heat treatment at 670 °C (Figure 1).

The initial $LiNi_{0.33}Mn_{0.33}Co_{0.33}O_2$ cathode powder consists of secondary particles about 4−10 μm in diameter, which are themselves composed of 0.2−0.5 μm primary particles (Figure 1a). When it is mixed with 40 wt % graphite and compacted into a pellet, a composite microstructure is observed, with cathode particles embedded in a matrix of graphite flakes (Figure 1b). Once the pellet is covered with the salts, a sharp interface between NMC-Gr and NaCl-KCl is visible, as there is no intermixing of the materials before heating (Figure 1c).

After heating to 670 °C, the interface becomes blurred because molten chlorides infiltrate the pellet (Figure 1f). Moreover, individual NMC particles are no longer clearly distinguishable at low magnification. At higher magnification, it becomes evident that the cathode material is porous and surrounded by solidified salt (Figure 1e). Only some particles have fully exposed surfaces (Figure 1d), indicating that the salt coating is relatively uniform and remains intact even after the pellet is cleaved for imaging.

The porous morphology of the cathode particles after heating with NaCl-KCl indicates that reduction occurs, even without a protective gas. A temperature of 670 °C is sufficient to melt the alkali chlorides, allowing them to infiltrate the pellet and shield the NMC-Gr mixture from the oxidative environment. To further clarify this process, EDX elemental maps were recorded at the interfacial region to analyze the distributions of various elements before and after the heat treatment (Figure 2).

Before heating, the Na−K−Cl and C−O−Ni−Mn−Co species are confined to the top and bottom parts of the images, respectively, creating a microstructure with a sharp interface between the pellet and the chloride eutectic (Figure 2a). However, after heating to 670 °C, the salts are detected not only above the phase boundary but also below it, occupying the entire space between the cathode particles (Figure 2b). At the same time, the transition metals are found only below the interface, and their outward diffusion is not noticeable, at least within the uncertainty limits of the EDX analysis.

It should be noted that after heat treatment at 670 °C the signal intensity decreases for all nonsalt constituents, especially for light elements. While before heating the O and C counts clearly outline the cathode material and graphite (Figure 2a), after heating their signals are significantly weaker (Figure 2b). Considering porous morphology of the particles, some oxygen and carbon might be consumed during reduction. However, a comparison of the sample weight before and after thermal treatment shows a loss of only 2 wt %, which does not appear sufficient to explain the pronounced drop in signal counts, particularly for carbon.

Moreover, optical microscopy reveals that the pellet fully retains its structural integrity even after heating (Figure S3). If most of the graphite had been consumed or burned, this would have resulted in a massive gas evolution and a complete rupture of the pellet. However, the top layer of the salt above the pellet contains only a few cavities, which suggests only minimal gas release. Therefore, the most reasonable explanation for the reduced signal intensity in EDX is the shielding effect of the salts. Upon melting, the chlorides infiltrate the pellet, resulting not only in the coverage of the cathode particles (Figure 1e), but also in the complete coating of the graphite flakes.

Although changes of the interfacial region between NMC-Gr and NaCl-KCl provide some insight into the reduction process, a deeper understanding of phase transformations is essential for analyzing the underlying mechanisms. To achieve this, a set of powdered samples made from the same starting materials was loaded into quartz capillaries (Figure S2), and temperature-resolved XRD patterns were collected during heating (Figure 3).

As indicated by the in situ data, at low temperatures the eutectic salt mixture consists of two crystallographic phases "KCl" and "NaCl" (Figure 3a). Hereinafter, the quotation marks are used to distinguish them from the respective pure chemical substances. Upon heating, the miscibility gap

https://doi.org/10.1021/acs.chemmater.5c02896
Chem. Mater. XXXX, XXX, XXX−XXX

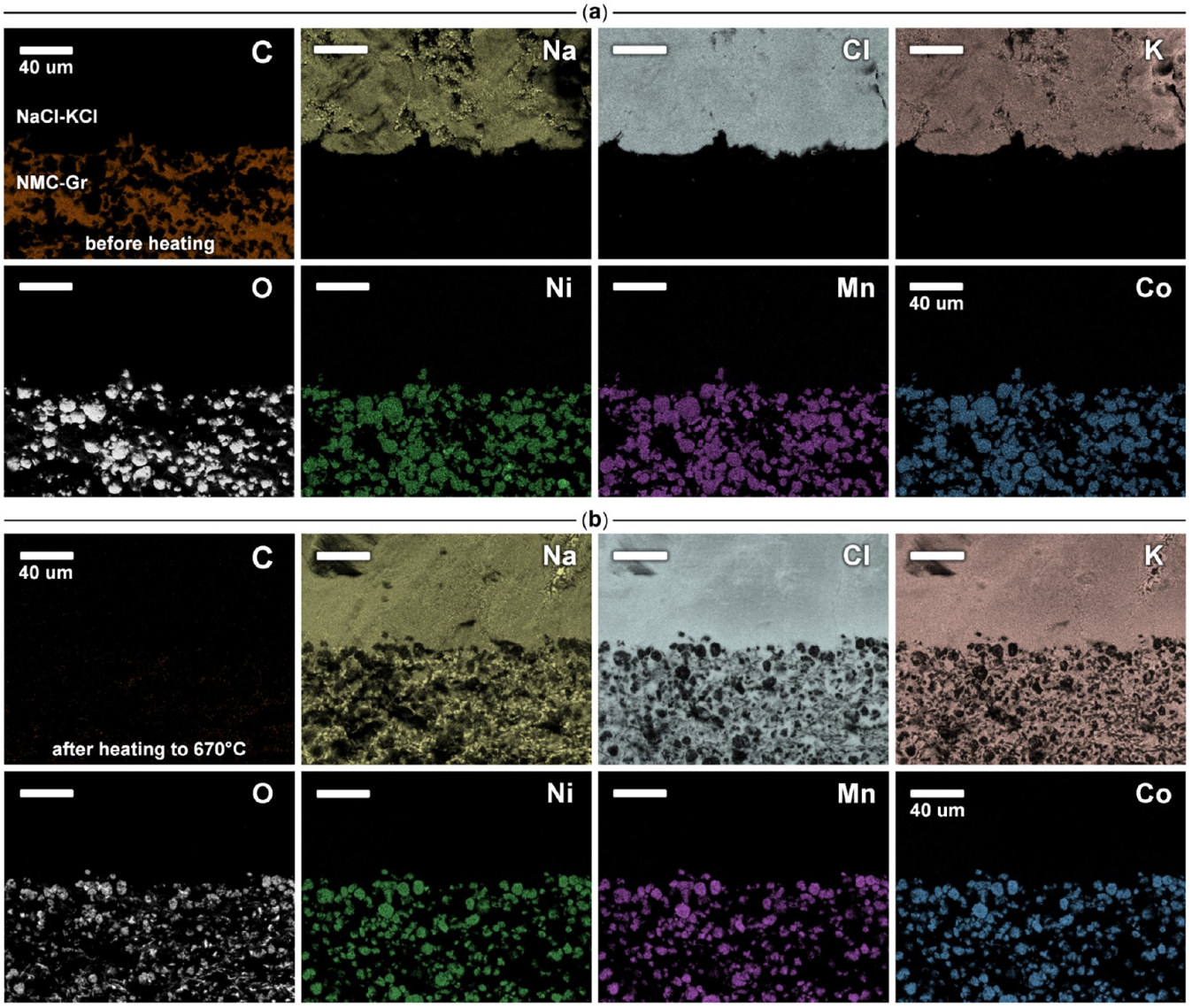

Figure 2. EDX elemental mapping of the interfacial regions between NMC-Gr and NaCl-KCl before (a) and after heating to 670 °C (b). Elements are shown in the order: C, Na, Cl, K, O, Ni, Mn, Co.

narrows, and the diffraction peaks of the two phases gradually merge starting from 350 °C, due to increasing intermixing of the components. A complete solid solution with a $Na_{0.5}K_{0.5}Cl$ composition forms above 500 °C and melts at 660 °C, which is consistent with the phase diagram.[33,34] This phase retains the original rock-salt structure of the parent compounds, but for visual clarity and to emphasize the fusion of the two salts, it is labeled as "$NaKCl_2$" in the graphs.

The $LiNi_{0.33}Mn_{0.33}Co_{0.33}O_2$ cathode material does not undergo any transformations within the studied temperature range when heated alone (Figure 3b). Only minor shifts of the diffraction peaks to lower angles are observed, attributed to anisotropic thermal expansion of the unit cell. When heated together with the eutectic salt (Figure 3c), there are also no apparent changes for the "NMC" structure aside from the lattice expansion. The chlorides merge into "$NaKCl_2$" and then melt, behaving similarly to when heated alone. A 1:2 mass ratio was used in this case to ensure an excess of salts, but no reaction occurred regardless.

The situation changes when the cathode material is heated not only with the chlorides but also with graphite (Figure 3d). Above 600 °C, the layered structure of "NMC" fully decomposes into a solid solution of cubic oxides, and the "$NaKCl_2$" phase melts shortly afterward. Above 650 °C, the peaks corresponding to a metallic *fcc* lattice emerge and then grow at the expense of the diminishing oxide phase. A 1:1 mass ratio was used to lower the intensity of the chloride peaks and enhance the visibility of oxides, whose reflections are weak and broad due to small crystallite sizes and the inhomogeneous intermixing of the three transition metals.

Since transformations of the cathode material are triggered only at elevated temperatures, a more detailed examination of this range is necessary. To facilitate this, a set of additional ex situ samples was prepared by covering NMC-Gr pellets with NaCl-KCl salts and heating them to 600−750 °C in a box furnace. After salt removal by washing, the resulting particles were imaged by SEM to correlate morphological changes with the evolution of the diffraction peaks (Figure 4).

https://doi.org/10.1021/acs.chemmater.5c02896
Chem. Mater. XXXX, XXX, XXX−XXX

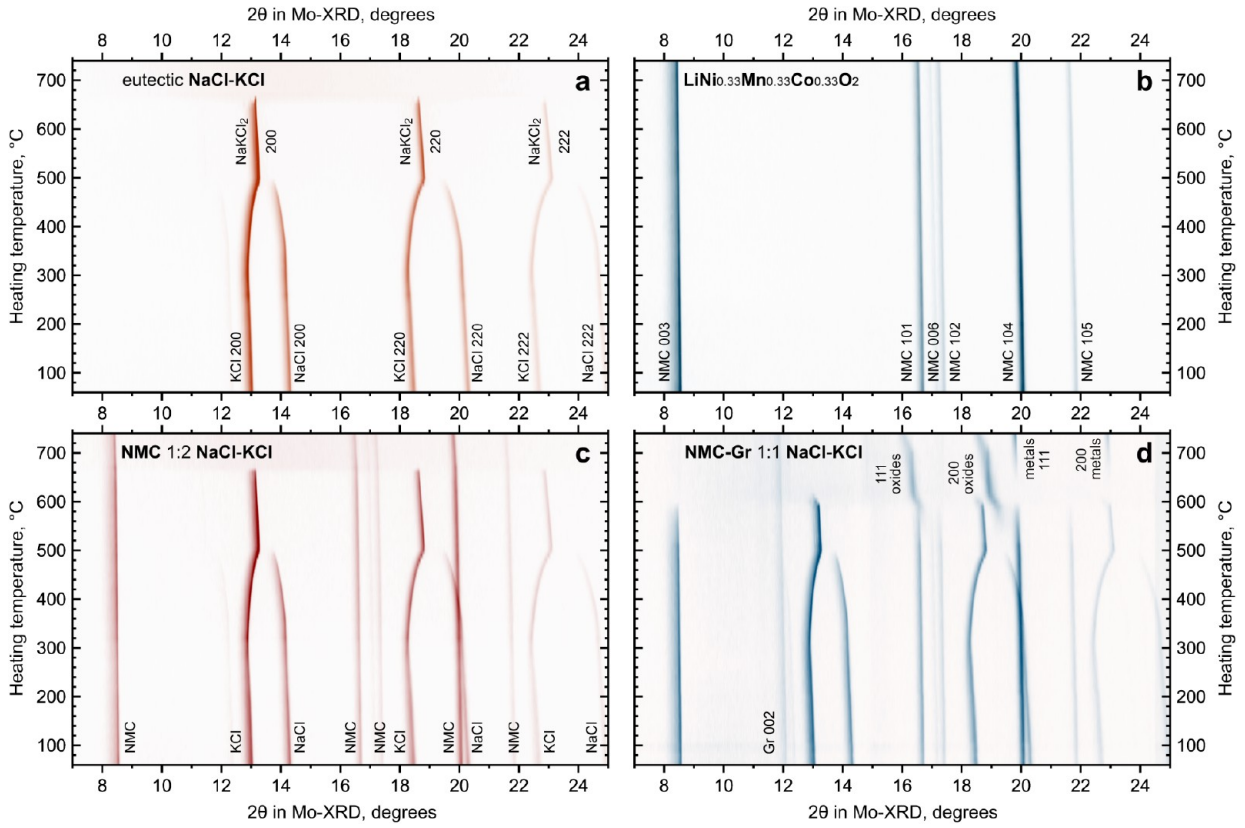

Figure 3. In situ XRD during heating of model material systems: NaCl-KCl eutectic only (a), $LiNi_{0.33}Mn_{0.33}Co_{0.33}O_2$ only (b), mixture of NMC and NaCl-KCl at a 1:2 mass ratio (c), mixture of NMC-Gr and NaCl-KCl at a 1:1 mass ratio (d).

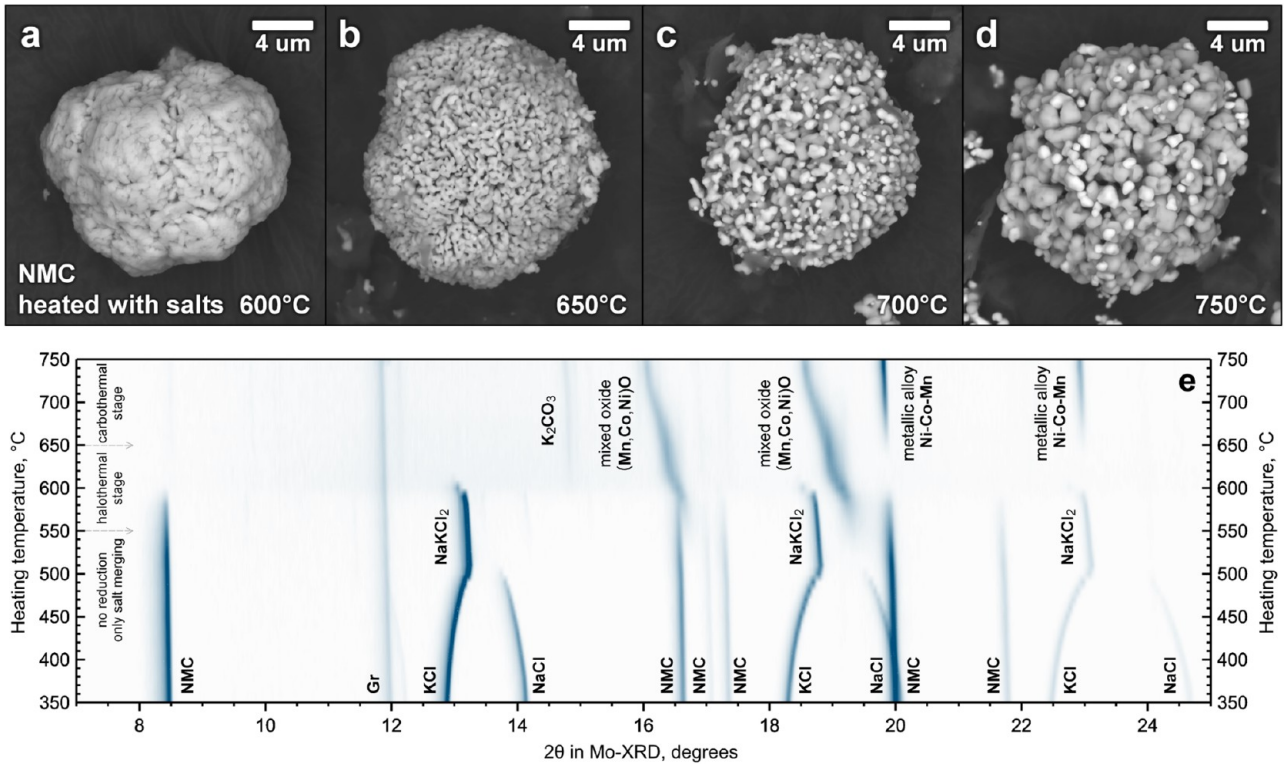

Figure 4. SEM images of ex situ NMC samples and corresponding in situ XRD data. Particle morphology after heat treatment with NaCl-KCl salts at 600 °C (a), 650 °C (b), 700 °C (c), and 750 °C (d), together with the diffraction patterns recorded during heating in the 350−750 °C range (e).

https://doi.org/10.1021/acs.chemmater.5c02896
Chem. Mater. XXXX, XXX, XXX−XXX

After heating to 600 °C, the NMC powder retains its initial morphology (Figure 4a). The only apparent variation is the growth of scale-like features on the surface of the particles, which are seen at higher magnification (Figure S4). However, this is likely unrelated to the reduction process and is simply a result of the washing and drying steps used to recover the insoluble fraction.[35,36] The change in morphology becomes visible after heating to 650 °C (Figure 4b), when some porosity forms inside the cathode particles. This indicates the onset of reduction, as the "NMC" phase disappears and "$NaKCl_2$" fully melts prior to 650 °C as follows from the in situ diffraction patterns (Figure 4e). At 700 °C, the pores become larger and some phase contrast emerges due to segregation of bright crystallites from the oxides (Figure 4c). At 750 °C, pores are further enlarged, but their number decreases because of grain growth and sintering of the particles (Figure 4d).

The comparison between the in situ XRD patterns and phase contrast in SEM images suggests that emerging bright crystallites correspond to the metallic *fcc* alloy. During reduction, it is likely that the transition metals migrate from the solid solution oxide into this alloy at different rates. This is inferred from the steady shift of the oxide peaks to lower angles in the 650−740 °C range. Since the lattice constants of pure NiO and CoO are smaller,[37] such a shift indicates a gradual increase in the MnO contribution, suggesting that nickel and cobalt are reduced to the metallic state first, while manganese is the last to convert. Interestingly, during the reduction of NMC622 (Figure S5), which contains more Ni and less Mn, the diffraction peaks of the mixed oxide gradually fade due to nucleation of the alloy, without any considerable shift to lower angles.

The increasing fraction of metallic alloy, which is observed in the in situ patterns above 650 °C (Figure 4e), represents the carbothermal stage of reduction. During this stage, oxygen from the solid solution oxide reacts with carbon from graphite, leading to gas evolution.[38,39] However, the "NMC" phase itself disappears by 600 °C, suggesting that an additional mechanism could be responsible for the collapse of the layered structure prior to carbothermal reduction.

Indeed, shallow diffraction peaks corresponding to the solid solution oxide phase are already visible at 550 °C (Figure 4e), indicating the onset of NMC decomposition. The initial positions of these peaks closely match those of NiO-CoO and then gradually shift to lower angles due to the incorporation of MnO. Therefore, manganese exsolves from the layered structure more slowly, consistent with its slower reduction during alloy formation at higher temperatures.

It is also worth noting that when NMC-Gr is heated without the salts but under an inert atmosphere, the nucleation of cubic oxides begins only at about 590 °C (Figure S6). Although this difference in the onset temperature is not large, it nevertheless suggests that chlorides facilitate the decomposition/reduction process. When this cathode material is heated with NaCl-KCl but without graphite, no reduction occurs at all (Figure 3c). Thus, the presence of both graphite and chloride eutectic is essential to enable the additional reduction mechanism.

The collapse of the initial NMC structure, even before reaching the carbothermal stage, can be explained by the following considerations. At 40 wt % content, the volume of graphite flakes is several times greater than that of NMC (Figure 1b), so cathode particles are therefore more frequently in contact with graphite than with the salts. Moreover, due to thermally activated intercalation,[40,41] graphite can act as a transport pathway for Li to diffuse out of the host material and encounter the nearest NaCl-KCl crystals. Given that K ions also intercalate into graphite at elevated temperatures,[42,43] lithium can exchange lattice sites with potassium in the rock-salt phase, especially once the chloride salts merge into "$NaKCl_2$".

It should be emphasized that such intercalation of alkali ions into graphite is driven by temperature,[40−43] and not by an electric field or potential, so it represents stochastic motion rather than directional transport. The thermal intercalation also implies that lithium and potassium may reside in a particular graphite flake only briefly before migrating to another host. Although Li and K do not intercalate within the same layer, as they preferentially form LiC_6 and KC_8 arrangements,[44] polycrystalline graphite in the form of flakes provides numerous pathways for the independent diffusion of both ions.

An important factor is that decomposition of NMC is observed starting from 550 °C, which coincides with the melting point of the LiCl-NaCl eutectic.[45,46] Below this temperature, lithium can exsolve from the chlorides, migrate back through graphite, and reincorporate into the NMC structure. However, above 550 °C, the migration of lithium ions into the salts becomes irreversible, as they are trapped within the local chloride melt.

The presence of a localized melt further promotes the intercalation,[47] allowing more K ions to leave the chloride crystals and create vacancies for lithium. At the same time, the size mismatch prevents potassium from dissolving into NMC, so it can instead bind with oxygen radicals from the cathode particles and promote oxidation of nearby graphite,[48] by forming the K_2CO_3 phase. Above 550 °C, this evolves into a cascade process, because migrated lithium no longer returns to the host cathode material, which progressively loses oxygen through interactions with potassium. As a result, the transition metals become partially reduced, and a solid solution of cubic oxides is formed. Hereinafter, this stage of reduction is referred to as *halothermal*. The term is inspired by the importance of halide salts in this type of interaction and is used to distinguish it from the carbothermal reduction, when the structural oxygen directly reacts with graphite at higher temperatures.

With regard to this additional reduction mechanism, a reasonable question is why it is not triggered at lower temperatures. The melting point of the binary LiCl-KCl eutectic is around 350 °C,[49] but thermal intercalation of lithium remains limited in this temperature range.[40,41] Even if some lithium ions were to diffuse far enough to reach neighboring chloride crystals, they would not accumulate in sufficient quantity near potassium ions to induce melting. Therefore, a more realistic scenario for an earlier onset of reduction would involve the localized formation of the ternary LiCl-NaCl-KCl eutectic, which melts below 550 °C.[50]

The formation of the ternary salt may be feasible if the carbon-based material allows sodium intercalation.[51] However, since Na intercalation into graphite is not favored,[52] the onset of reduction aligns closely with the LiCl-NaCl melting point. Nonetheless, the halothermal stage of reduction could be triggered earlier if a considerable fraction of cathode particles is in contact not only with graphite but also with the chlorides. This could facilitate the formation of the ternary eutectic at the triple-phase boundaries and lower the effective melting point of the salt.

https://doi.org/10.1021/acs.chemmater.5c02896
Chem. Mater. XXXX, XXX, XXX−XXX

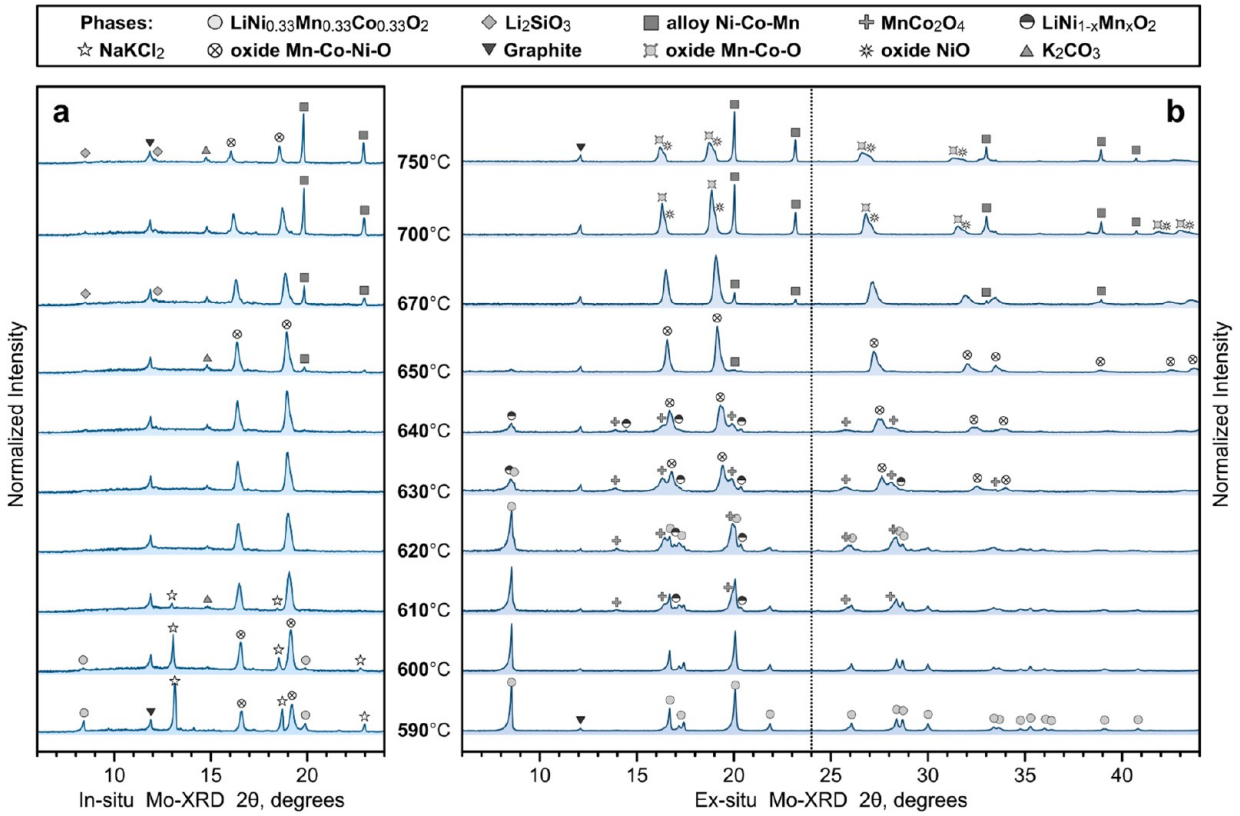

Figure 5. Comparison of in situ and ex situ XRD for NMC-Gr with NaCl-KCl: patterns at high temperatures in quartz capillaries (a) and room-temperature scans after washing of samples annealed in alumina crucibles (b). The dashed line in the ex situ patterns indicates the corresponding range of the in situ scans.

While the halothermal reduction of NMC-Gr is observed above 550 °C in capillaries, it remains unclear why the particle morphology is retained when the pellets are heated to 600 °C. Therefore, it is of practical importance to understand the factors influencing onset of the reduction process. To address this, a set of ex situ samples was heat-treated at 590−750 °C, washed to remove the salts, and then the resulting powdered materials were analyzed by XRD to determine the phase composition and allow direct comparison with the in situ diffraction patterns (Figure 5).

In the 650−750 °C range, both in situ and ex situ patterns for the most part demonstrate similar phases, with a gradual conversion of oxides to metals during the carbothermal stage of reduction. Nonetheless, a few minor differences between the two data sets are worth noting. At high temperatures, a complete solid solution of MnO, CoO, and NiO is observed (Figure 5a), whereas at room temperature, a right shoulder on the diffraction peaks indicates the exsolution of nickel oxide from the mixture (Figure 5b). This feature reflects the temperature dependence of mutual solubility, suggesting that these oxides are less likely to remain as a solid solution upon cooling if some fraction of transition metals is already in the alloy. Another distinction is the presence of Li_2SiO_3 traces in the in situ patterns, resulting from a side reaction between lithium and the quartz capillary above 650 °C (Figure S7). The ex situ samples are heated in alumina crucibles, and no such phase is detected due to the absence of a silicon dioxide source.

Below 650 °C, more pronounced variations are observed in the XRD patterns of in situ and ex situ samples. In quartz capillaries, the "NMC" phase decomposes into a solid solution oxide by 600 °C, even before "$NaKCl_2$" is fully molten at 620 °C, and no further changes are detected until the metallic alloy begins to nucleate at 650 °C (Figure 5a). For the pellets heated in crucibles, the decomposition occurs more gradually via the segregation of several intermediate phases in the 610−650 °C range. Specifically, small diffraction peaks of $LiNi_{1-x}Mn_xO_2$ and $MnCo_2O_4$ emerge at 610 °C and then grow further between 620 and 640 °C. The solid solution oxide appears only at 630 °C, but it becomes the dominant phase by 650 °C (Figure 5b).

Another notable difference is the presence of K_2CO_3 in the in situ patterns (Figure 5a). The formation of this carbonate phase is consistent with the proposed mechanism of halothermal reduction. Once lithium diffuses through graphite and exchanges lattice sites with potassium in chloride crystals, K ions are unable to incorporate into cathode particles and instead react with oxygen radicals and carbon. In the absence of graphite, this reaction is not favorable (Figure 3c), as there is no medium to facilitate the lithium migration from NMC into NaCl-KCl.

For the both types of samples, traces of the metallic alloy become visible only above 650 °C (Figure 5a and b), indicating that the carbothermal stage of reduction for the cathode material is initiated at this temperature threshold. However, the onset of the halothermal stage is delayed only in the ex situ experiments. The photographs taken after crucible removal from the furnace show that salt melting begins at a slightly higher temperature than in the in situ case (Figure S4), which coincides with a slower decomposition rate of the "NMC" phase. This suggests that the onset of halothermal reduction is closely related to the actual melting point of the

https://doi.org/10.1021/acs.chemmater.5c02896
Chem. Mater. XXXX, XXX, XXX−XXX

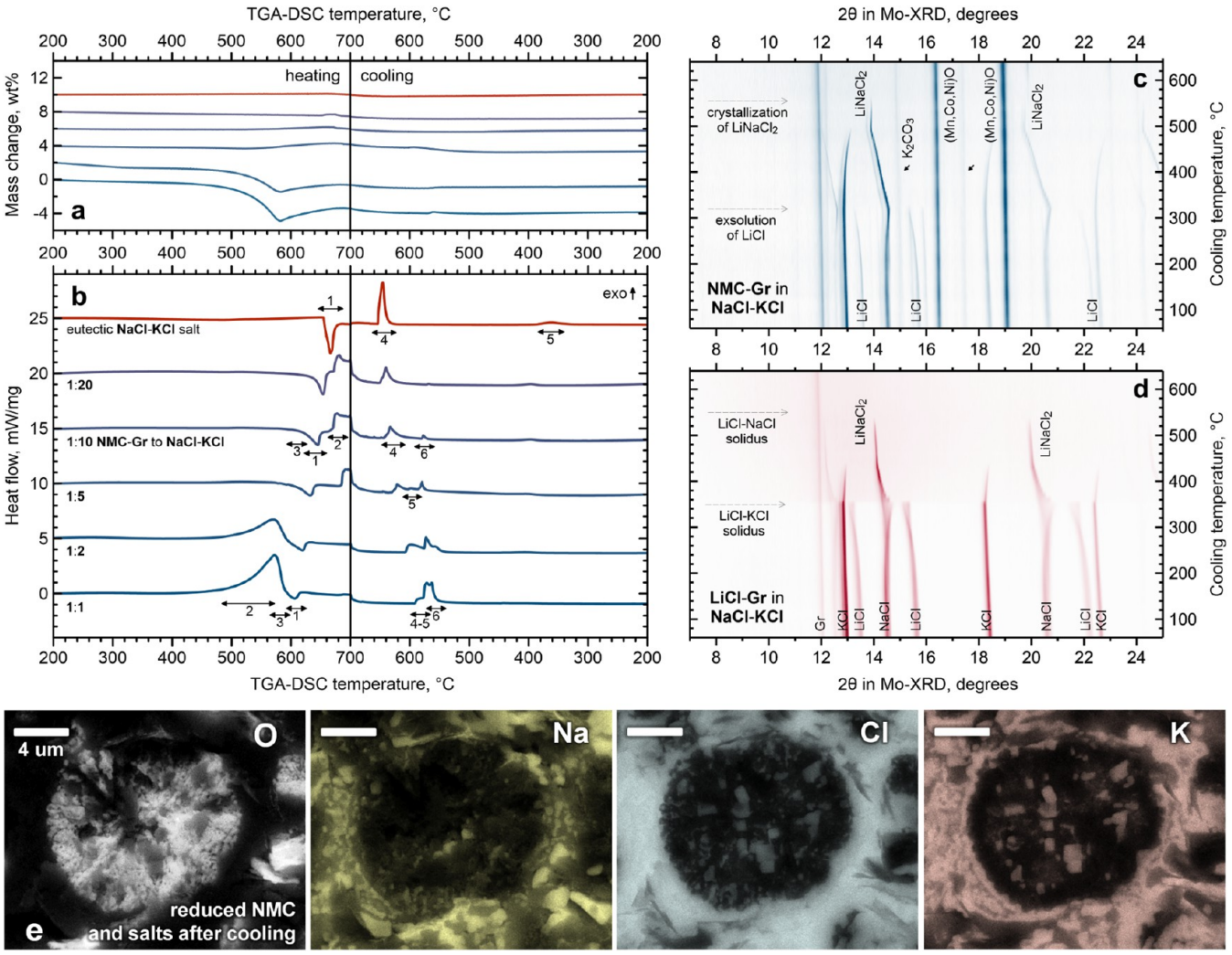

Figure 6. Effect of lithium migration on the behavior of chloride salts. TGA-DSC for different mass ratios of NMC-Gr to NaCl-KCl (a, b), in situ XRD during cooling of a sample with a 1:1 ratio and a model ternary chloride system (c, d), and EDX elemental mapping of solidified salt containing a reduced particle after heat treatment at 670 °C (e).

chloride eutectic. One of the differences between the in situ and ex situ samples was the mass ratio of NMC-Gr to NaCl-KCl, which was set at 1:1 for capillaries and 1:10 for pellets. For the sake of consistency, it would have been ideal to use the same ratio for both cases, but it was not feasible in practice. A larger amount of salt was required to fully cover the NMC-Gr pellet in a large alumina crucible compared to small quartz capillaries. Conversely, a high fraction of salt would have made it difficult to detect the oxide and alloy phases during in situ XRD due to the strong intensity of the NaCl-KCl peaks.

To investigate whether the mass ratio affects the melting behavior, a set of samples was prepared for TGA-DSC analysis by varying the relative content of NMC-Gr with respect to NaCl-KCl. In addition, the in situ XRD patterns were recorded during cooling to support the interpretation of heat effects, and the ex situ pellet with solidified salt and reduced particles was characterized by EDX to gain further insight into the interaction between the chloride salts and lithium (Figure 6).

The NaCl-KCl eutectic shows an endothermic peak at around 660 °C (Figure 6b), which is consistent with the literature data.[53] For clarity, various heat effects on the DSC curves are labeled with numbers, with effect **1** corresponding to the chloride melting. When NMC-Gr is gradually added, the position of this effect steadily shifts to lower temperatures. It appears at 650 °C for a 1:10 ratio, used for the ex situ samples, and at 600 °C for a 1:1 ratio, used in the in situ case. For intermediate ratios, the melting temperature falls between these values, directly confirming that higher NMC content leads to a greater decrease in melting point, driven by lithium migration into the salts. Notably, no other endothermic peaks associated with the carbothermal reduction are observed, as this stage is not reached during dynamic heating to 700 °C, and only the halothermal reduction occurs under these conditions.

The heat effect labeled as **2** is attributed to instrumental aspects of the analysis (Figure 6b), as each measurement involves placing a 3 mm pellet is placed into a 6 mm crucible. The complete crucible filling is not feasible, since molten chlorides could escape due to wetting of the alumina surface. Because of the small pellet size, it is not possible to embed the cathode material and graphite inside, as is done for ex situ samples. Instead, all constituents are intermixed, similarly to the experiments with capillaries. It does not affect the pure NaCl-KCl eutectic, but for 1:20, 1:10, and 1:5 mass ratios, a slight dip in the TGA curves occurs shortly after melting, when some graphite flakes become exposed and begin to oxidize

https://doi.org/10.1021/acs.chemmater.5c02896
Chem. Mater. XXXX, XXX, XXX−XXX

(Figure 6a). At higher contents of NMC-Gr, graphite accounts for the largest volume fraction and is significantly exposed to air, leading to pronounced oxidation, reflected in the exothermic effect starting from 480 °C. Nonetheless, effect **2** is not significant in the in situ and ex situ experiments, since graphite is not exposed to the oxidative environment to the same extent as in the TGA-DSC samples.

To interpret the heat effects during cooling, it is helpful to examine the corresponding in situ XRD patterns for NaCl-KCl with NMC-Gr and compare it to the case of LiCl-Gr (Figure 6c and d). For this ternary chloride mixture, the content of LiCl was selected such that the lithium concentration matched that of NMC-Gr mixed in a 1:1 ratio with the binary eutectic. In both cases, the diffraction peaks for the "$LiNaCl_2$" phase are observed from about 540 to 360 °C, representing the solid solution of NaCl and LiCl.[54] Moreover, since "$LiKCl_2$" does not form due to a large difference in the cation size,[49] a portion of potassium remains in the LiCl-KCl melt until about 350 °C. Below this temperature, a separate "LiCl" phase emerges, and the intensity of the "KCl" peaks increases.

The understanding of the solidification products facilitates interpretation of the DSC curves during cooling (Figure 6b). The pure eutectic crystallizes into "$NaKCl_2$" below 640 °C and dissociates into separate "NaCl" and "KCl" below 420 °C (Figure S7). The corresponding exothermic effects are labeled as **4** and **5**, respectively. When NMC-Gr is added, an additional exothermic peak emerges at 550 °C, labeled as effect **6**, which is attributed to the crystallization of "$LiNaCl_2$", based on the characteristic temperature.[46] For the 1:20 and 1:10 ratios, these three effects are clearly separated, but for the 1:5 ratio, heat effect **4** is closely followed by effect **5**, indicating that "$NaKCl_2$" dissociates into separate salts shortly after solidification.

The crystallization of a solid solution between NaCl and KCl becomes less favorable at higher NMC-Gr content, so the intensity of heat effects **4** and **5** steadily decreases, whereas effect **6** becomes more pronounced. Moreover, at 1:2 and 1:1 ratios, effects **4** and **5** overlap, suggesting that "$NaKCl_2$" crystallizes and dissociates almost simultaneously, thereby releasing NaCl to form the solid solution with LiCl. As a result, the "$LiNaCl_2$" phase is observed in the in situ patterns below 550 °C (Figure 6c), and its dissociation below 350 °C does not produce a distinct heat effect due to slow kinetics (Figure 6d).

Given the impact of lithium on the solidification of salts, heat effect **3** can intuitively be associated with its migration into the chloride phase during heating. As this migration occurs just before melting, it strongly overlaps with heat effect **1**, which is visible starting from the 1:10 ratio (Figure 6b). The pure NaCl-KCl eutectic shows a normal melting peak, after which the curve shifts due to a change in heat capacity. However, the addition of NMC-Gr causes lifting of the left side of the peak, as lithium migration is exothermic,[55] while salt melting is endothermic.

The solidification of the LiCl-KCl eutectic at 350 °C, which is clearly visible for the ternary chloride mixture (Figure 6d), is less apparent for NaCl-KCl with NMC-Gr. Nonetheless, a characteristic change can still be observed in the in situ XRD patterns at the same temperature (Figure 6c), representing the dissociation of "$LiNaCl_2$" into "LiCl" and "NaCl". Below the solidus at 340 °C, some oxychloride phases emerge in the in situ XRD patterns (Figure 6c), but their peak intensities are rather low. Nevertheless, the segregation of competing phases is driven by chloride-deficiency, which is not significant in the ex situ samples with higher salt content.

The existence of solid solution between LiCl and NaCl during solidification is consistent with the proposed mechanism of halothermal reduction. Upon heating, lithium diffuses through graphite and replaces potassium in the rock-salt lattice, effectively dissolving in the salts. Upon cooling, lithium partially crystallizes from the melt as the "$LiNaCl_2$" phase. Both steps are thermodynamically favorable, with formation enthalpies of 4.93 kJ/mol for "$NaKCl_2$" and 3.05 kJ/mol for "$LiNaCl_2$".[55] This indicates that replacing K with Li in the salt crystals lowers the total energy of the alkali chlorides. Nonetheless, when salt content is high relative to the cathode material and graphite, as in the ex situ samples, the amount of formed "$LiNaCl_2$" should be smaller compared to "$NaKCl_2$" due to the lower concentration of available lithium.

For additional characterization of the salt after cooling, the area surrounding the reduced particle was analyzed by EDX (Figure 6e). The distribution maps for Na and K reveal lighter and darker regions that do not fully coincide with Cl, implying a slight dilution of the chloride salts due to the presence of "LiCl". Moreover, the concentration of sodium is very low near the particle surface and at the core, as it does not intercalate into the graphite around the cathode material. This is not an artifact of the specific data set and can also be observed in other parts of the NMC-Gr pellet heated with the NaCl-KCl salts (Figure S8). Therefore, such features provide additional evidence for the halothermal mechanism of reduction.

Since the amount of chloride ions in the system is limited, a portion of potassium remains locked in the carbonate phase during cooling. The EDX mapping of K and Cl shows that these elements do not completely overlap at the particle core, suggesting the most probable location of "K_2CO_3" (Figure 6e). This carbonate phase is poorly soluble in the chloride melt and therefore is not expected to diffuse far from its point of formation. The remaining potassium partially crystallizes as "KCl" below 490 °C and partially persists in the LiCl-KCl melt down to 350 °C. The presence of a molten potassium-containing phase over a broad temperature range results in a uniform distribution of this chloride around the cathode material. This is evident from the K and Cl signal counts, which outline the wavy contours of transition metal oxides. In contrast, sodium is less abundant in the vicinity of the reduced particle (Figure S8), as it does not intercalate into graphite during heating and begins to crystallize earlier during cooling, starting at 550 °C.

The halothermal reduction and the corresponding migration of lithium from the cathode material into the chloride salts have direct implications for the recycling of battery waste. To quantify the Li recovery rate, the NMC-Gr pellet mixed with NaCl-KCl in 1:10 mass ratio was heated to 670 °C and then dissolved in deionized water, followed by centrifugation to separate the saline solution from the insoluble transition metal oxides and graphite. According to the ICP-OES analysis, the recovered liquid contains most of the lithium from the initial cathode material (Table S1). Therefore, alkali chloride salts not only enable the reduction process without the need for protective gases but also ensure the subsequent extraction of lithium.

Considering the potential benefits, it is of great interest to verify the applicability of the proposed method to other common cathode materials that may be present in the Li-ion battery waste and black mass. For this purpose, the samples

https://doi.org/10.1021/acs.chemmater.5c02896
Chem. Mater. XXXX, XXX, XXX−XXX

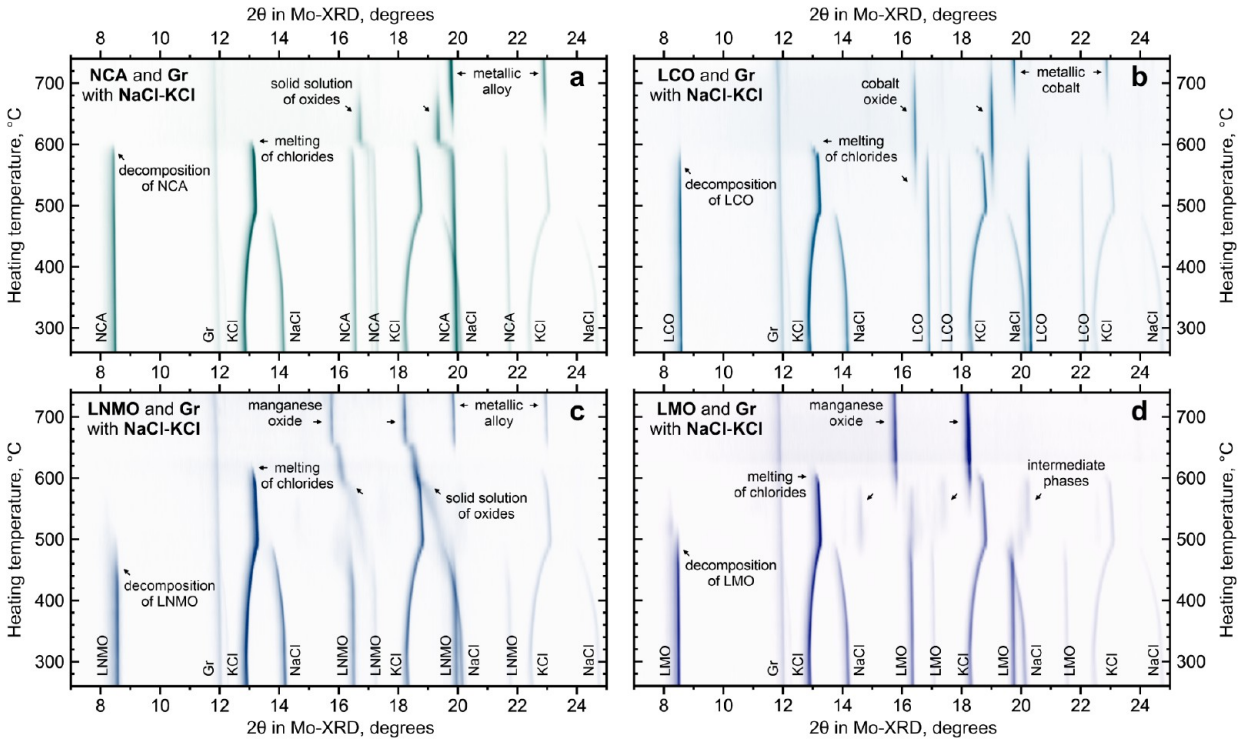

Figure 7. In situ XRD during heating of common cathode materials mixed with graphite and NaCl-KCl salts: $LiNi_{0.80}Co_{0.15}Al_{0.05}O_2$ (a), $LiCoO_2$ (b), $LiNi_{0.5}Mn_{1.5}O_4$ (c), and $LiMn_2O_4$ (d).

containing $LiNi_{0.80}Co_{0.15}Al_{0.05}O_2$, $LiCoO_2$, $LiNi_{0.5}Mn_{1.5}O_4$, and $LiMn_2O_4$ particles were prepared following the same protocol as for NMC, each mixed with graphite and NaCl-KCl, and then analyzed by in situ XRD.

As seen from the temperature-resolved patterns, very similar behavior of the chloride salts is observed in all four cases (Figure 7), which also aligns with the data for equimolar NMC and NMC622. Starting from 350 °C, the diffraction peaks for "NaCl" and "KCl" gradually merge due to increasing intermixing, until the solid solution "$NaKCl_2$" forms at 500 °C and melts above 600 °C. Nonetheless, the onset of reduction depends on the cathode composition.

In the $LiNi_{0.80}Co_{0.15}Al_{0.05}O_2$ case (Figure 7a), the intensities of the "NCA" peaks begin to decrease at 580 °C. By 610 °C, the initial layered structure decomposes into a solid solution of NiO-CoO oxides due to lithium migration. After melting of the chloride salts, the metallic Ni−Co alloy nucleates at 620 °C and becomes the dominant phase by 700 °C. The residual aluminum is likely also dissolved in the alloy, as no other secondary phases are observed. In contrast to NMC, the halothermal stage of reduction for NCA occurs in a narrower temperature range, and the carbothermal stage is triggered earlier.

The behavior of $LiCoO_2$ is similar to that of equimolar NMC and NMC622 in terms of the onset of various reduction stages (Figure 7b). The cubic oxide emerges at 530 °C along with a simultaneous fading of the "LCO" peaks, as lithium begins to migrate from the host structure. The chloride salts are fully molten at 610 °C, but further reduction of CoO is initiated only at 650 °C. By 740 °C, this oxide phase is completely converted into metallic Co.

Compared to the layered cathode materials, the decomposition of the spinel compounds occurs at lower temperatures. For $LiNi_{0.5}Mn_{1.5}O_4$ (Figure 7c), the "LNMO" phase starts to fade at 450 °C, and by 520 °C it gradually dissociates into $LiMnO_2$ and NiO-MnO due to partial lithium loss. Above 530 °C, lithium continues to migrate into NaCl-KCl, while the diffraction peaks of the solid solution oxide steadily shift to lower angles. This peak shift is associated with the decomposition of $LiMnO_2$ and the incorporation of additional manganese into the oxide mixture. The chloride salts are molten at 630 °C, and the Ni−Mn alloy begins to nucleate due to further reduction of the oxides. Above 670 °C, the oxide peaks become sharper and no longer shift, indicating that all Ni is already in the metallic form and minimal conversion occurs for the remaining MnO.

The $LiMn_2O_4$ cathode powder mostly resembles the LNMO case, but without the formation of a solid solution oxide (Figure 7d). The decomposition of "LMO" begins at 480 °C through the formation of intermediate phases $LiMnO_2$ and Mn_3O_4 because of partial lithium loss. Above 540 °C, the MnO peaks emerge due to additional migration of lithium into the chloride salts, which are fully molten at 630 °C. In contrast to the other tested materials, no further reduction is observed after salt melting, and MnO remains the dominant phase up to at least 740 °C.

The obtained in situ XRD patterns demonstrate that the halothermal stage of reduction for the spinel cathode materials proceeds over a broader temperature range, during which they gradually decompose into $LiMnO_2$ and Mn_3O_4 or NiO-MnO mixture. At the same time, the carbothermal stage is less pronounced, as manganese oxides react poorly with carbon from the graphite flakes. Therefore, a temperature of 650 °C can be considered as a safe choice for the reduction of real black mass containing different cathode chemistries. At this temperature, the halothermal stage is completed for all common materials, and they decompose into porous transition metal oxides. Above 650 °C, metallic crystallites grow during

https://doi.org/10.1021/acs.chemmater.5c02896
Chem. Mater. XXXX, XXX, XXX−XXX

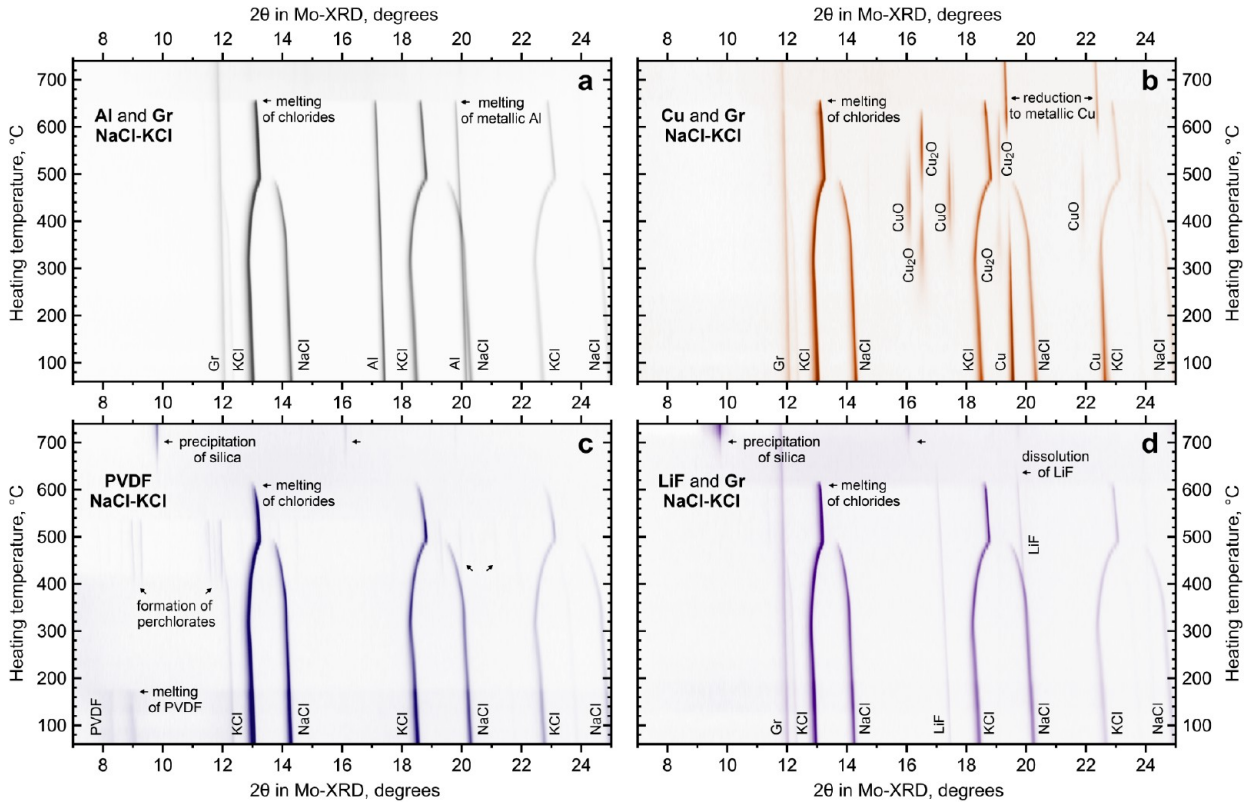

Figure 8. In situ XRD during heating of typical black-mass impurities mixed with NaCl-KCl: Al (a) and Cu (b) current collectors with graphite, PVDF binder (c), and LiF with graphite (d).

the carbothermal stage, leading to graphite consumption, which is not necessary for the extraction of lithium and separation of transition metals.

The earlier onset of halothermal reduction for the spinel compounds compared to the layered materials is probably associated with the smaller size of secondary particles. According to the specifications provided by Sigma-Aldrich, both the LNMO and LMO powders have an average size of about 1 μm. Therefore, as previously suggested, a high count of triple-phase boundaries, where the cathode material is in contact with graphite and chloride salts, could lower the temperature of irreversible lithium migration below 550 °C. While such a decrease is difficult to achieve with larger layered particles, it is feasible for finely dispersed spinel cathodes, whose volume is comparable to that of graphite flakes.

It is worth noting that another widely used cathode material, $LiFePO_4$, does not appear to be suitable for treatment with NaCl-KCl. In the 320−520 °C range, it gradually decomposes into $Li_3Fe_2(PO_4)_3$ with partial segregation of Fe_2O_3, but then recrystallizes into its initial olivine structure above 530 °C due to the carbothermal reduction (Figure S9). Therefore, if black mass contains LFP particles, it requires a different processing strategy compared with the spinel or layered compounds.

As the transformations of various cathode materials during the heat treatment with alkali chlorides are clarified, it is also of practical importance to understand the behavior of typical impurities that could be present in black mass. Therefore, in situ samples containing Al, Cu, PVDF, and LiF powders were prepared, and temperature-resolved XRD patterns were recorded in the same way as for different cathode compositions discussed above (Figure 8).

To analyze the behavior of Al and Cu, often present as inclusions of current collectors, a 1:3 mass ratio to NaCl-KCl was used to ensure that the intensities of the metal peaks remained visible relative to the salts. In the case of aluminum, no interactions between the constituents are observed until 660 °C, at which point it melts simultaneously with the chlorides (Figure 8a). In contrast, copper shows a sequence of phase transitions with increasing temperature (Figure 8b). At 250 °C, it begins to oxidize to Cu_2O, followed by further conversion to CuO at 350 °C. Starting from about 500 °C, copper is reduced to Cu_2O through the reaction with carbon, and then transforms into the metallic form by 620 °C, even before the salts melt.

An important practical outcome is that when Al and Cu are present in NMC-Gr or black mass prior to heat treatment, they do not migrate into the chloride melt and fully remain in the insoluble fraction (Figure S10). Moreover, an interesting side effect is observed when both metals are heated above 660 °C (Figure S11), as melting of aluminum triggers the nucleation of an intermetallic compound with copper. The content of iron in black mass is typically very low due to magnetic separation of steel pieces,[56] but if such an impurity is present, it could also participate in the side reactions. Therefore, the formation of minor intermetallic phases is possible when black mass is heated to or above the melting point of aluminum.

The PVDF binder, which is used to adhere cathode particles and graphite to Al and Cu current collectors, respectively, melts at around 180 °C and remains in this state up to 420 °C (Figure 8c). Due to its low average atomic number, it was mixed with NaCl-KCl in 1:2 mass ratio to improve visibility. Once this polymer decomposes, the diffraction peaks corresponding to sodium and potassium perchlorates appear

https://doi.org/10.1021/acs.chemmater.5c02896
Chem. Mater. XXXX, XXX, XXX−XXX

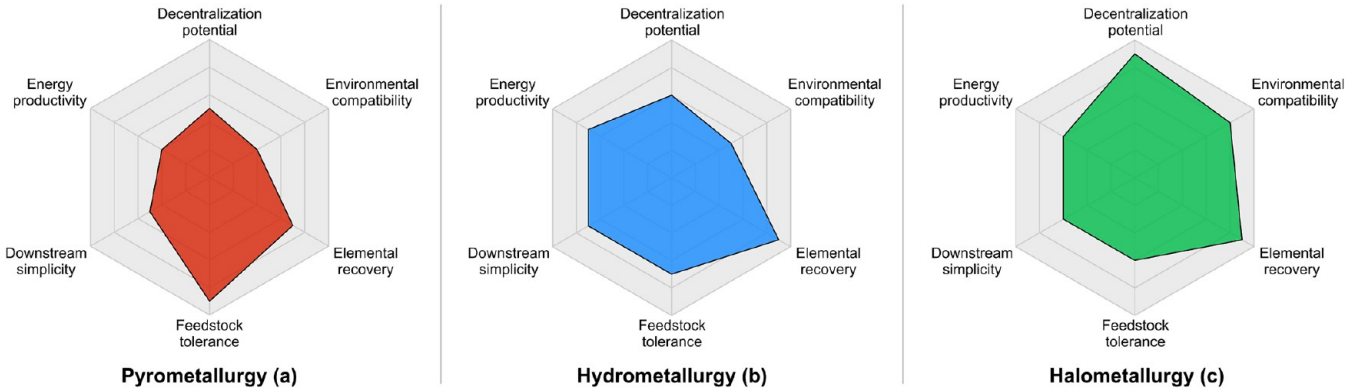

Figure 9. Radar diagrams for techno-economic comparison of battery recycling routes: pyrometallurgy (a), hydrometallurgy (b), and halometallurgy (c). Radial axes increase from the center (low) to the edge (high), indicating the relative levels of each parameter.

in the 430−540 °C range. These most likely represent fluorinated variants of the perchlorate phases rather than pure compounds. The capture of fluorine by the salts becomes more evident at higher temperatures, since it lowers the melting point of "$NaKCl_2$" to 610 °C. Shortly after melting, the SiO_2 phase emerges as presence of fluorine in the melt promotes dissolution of quartz,[57] which then precipitates in powdered form.

A nearly identical degradation of quartz glass is observed when LiF-Gr is mixed with NaCl-KCl in a 1:8 mass ratio and then heated (Figure 8d). The LiF impurity often originates from the decomposition of $LiPF_6$ (Figure S9), which occurs during the drying of shredded battery waste to evaporate electrolyte solvents. It not only lowers the melting point of "$NaKCl_2$" to 610 °C, but also dissolves in the melt at 630 °C, causing the precipitation of silica. Although such corrosion of capillaries is merely an artifact of the measurement setup, it directly indicates the presence of fluorine in the molten salts. Given the low content of PVDF and LiF in industrial black mass,[58,59] it is reasonable to expect that all fluorine could be trapped by the chloride salts during the heat treatment.

After examining various cathode compositions and typical impurities, it is also necessary to verify that the proposed treatment is equally effective for real battery waste. To this end, industrial black mass was compacted into a disk-shaped pellet, covered with NaCl-KCl, and then heated to 670 °C. Under these conditions, the main products are identical to those obtained for the model NMC-Gr mixture, namely a solid solution of transition metal oxides and graphite (Figure S12). The traces of Al- and Cu-based compounds are also observed, as these impurities are commonly present in this type of waste. Another useful outcome is that alkali chlorides can be reused for the reduction process over multiple cycles, with lithium continuing to migrate into the salts even without intermediate delithiation after each run (Figure S13).

The results presented in this study demonstrate that treatment of battery materials with chloride salts is highly relevant for black mass handling and recycling. The proposed process does not require a protective atmosphere and can be performed under ambient air. It also aligns with the emerging recycling paradigm that relies on various molten salts for processing battery waste.[60,61] By analogy with pyrometallurgy and hydrometallurgy, this approach can be classified as *halometallurgy*, because it is based on interactions between target materials and halide compounds. This terminology is consistent with the observed mechanism of halothermal reduction, in which lithium ions migrate from the cathode particles into chloride crystals via thermal intercalation and diffusion through graphite.

A comparison between the proposed method and other two conventional battery recycling techniques, pyrometallurgy and hydrometallurgy, is summarized using radar diagrams (Figure 9), which highlight the most relevant techno-economic parameters. One of the notable outcomes is the strong decentralization potential of halometallurgy. Due to the relative simplicity of the processing steps, this approach could be implemented across a wide range of scales, enabling small- and medium-sized companies to process the battery black mass and thereby promoting the decentralized recycling market. In contrast, the pyrometallurgical and hydrometallurgical approaches are viable only at high processing tonnage and therefore require large centralized facilities.[14,15] These methods are also associated with lower environmental compatibility, leading to substantial costs for ensuring safe operation for both personnel and the environment. By comparison, halometallurgy avoids excessively high temperatures, does not require a controlled gas atmosphere, does not involve acids, and suppresses fluorine emissions from the binder decomposition.

The products of halometallurgy require further downstream treatment, as both lithiated chloride salts and transition metal oxides must be additionally processed to reintegrate the Li, Ni, Mn, and Co precursors into the economy. Importantly, this requirement also applies to other techniques, because transition metal sulfates and lithium carbonate should be purified after hydrometallurgy, and pyrometallurgical slag should be subjected to leaching. In this context, halometallurgy offers greater flexibility in downstream material flow, as its decentralization supports adaptable and locally distributed processing strategies.

The saline solution obtained after treatment of black mass with alkali chlorides can be referred to as *halothermal brine*, emphasizing that lithium migrated into the salts as a result of halothermal reduction. The composition of this solution is comparable to that of continental brines, indicating that it could be processed using the methods of direct lithium extraction, collectively known as DLE, to obtain Li_2CO_3, LiOH, or LiCl compounds.[62]

Among the DLE techniques developed over the past two decades,[63,64] the membrane separation and electrochemical recovery appear particularly suitable, as they facilitate the reuse of chlorides after delithiation. Moreover, in contrast to natural lithium-rich brines, halothermal brine does not contain calcium

https://doi.org/10.1021/acs.chemmater.5c02896
Chem. Mater. XXXX, XXX, XXX−XXX

and magnesium ions, which are detrimental to certain extraction techniques.

The insoluble fraction after halometallurgy, consisting mostly of porous oxide particles and graphite, can be converted into soluble products either by advanced hydrometallurgy,[65] or by annealing with the corresponding ammonia salts.[60] Alternatively, if metallic impurities are washed away and graphite is removed by flotation,[66] the solid solution of transition metal oxides can be used as a precursor for all-dry synthesis of cathode materials.[67] Such synthesis protocols are closely related to the direct recycling or even upcycling of spent cathode powders and the growth of single-crystal particles.[68−70]

The elemental recovery rates achieved by halometallurgy are relatively high, as the transition metals do not diffuse into the chloride melt and remain entirely in the insoluble fraction. Nevertheless, lithium migration into the melt could be further enhanced by adjusting the spatial distribution of black mass and salts (Figure S14). For example, when the pellet itself contains not only cathode material and graphite but also embedded salts, the lithium content in the saline solution increases from 91% to about 96% (Table S1). The presence of salt within the pellet shortens the diffusion path for lithium to reach the chlorides during heating and also mitigates its reincorporation into the oxide phase during cooling.

The feedstock tolerance of halometallurgy is lower than that of pyrometallurgy, because it requires a fine black mass rich in Ni−Mn−Co metals and ideally free of LFP inclusions. In contrast, batteries with diverse cathode chemistries can be processed through the smelter route regardless of their condition. The energy productivity of the proposed method is also lower than that of hydrometallurgy, as it inherently involves thermal treatment. However, more efficient inductive furnaces could potentially improve this parameter in the future.

Although the radar diagrams provide only a qualitative comparison between the three recycling techniques, a detailed techno-economic analysis is currently not feasible due to the low technological readiness of halometallurgy. This study serves as proof of concept, with a primary focus on the underlying scientific principles. Further optimization and process customization, particularly at the engineering level, will likely be required before widespread commercial adoption takes place.

To facilitate the practical implementation of halometallurgy, an important guideline can be formulated. While both halothermal and carbothermal stages of reduction are discussed in this work, the halothermal reduction alone is sufficient for cathode decomposition and lithium migration into the chloride salts. Therefore, it is not necessary to raise the temperature above 650 °C, although additional tuning of the thermal profile within the 600−650 °C range may be beneficial for suppressing side reactions involving current collector inclusions.

Overall, the simplicity of the process, in combination with its distinct mechanistic basis, may allow halometallurgy to establish a niche and contribute to the decentralization of battery recycling. This is particularly relevant in the context of the ongoing energy transition and the growing demand for electrochemical energy storage. Beyond battery waste, the creation of quasi-inert conditions under ambient air has academic value in its own right and could find application in other material systems.

4. CONCLUSIONS

The present study experimentally demonstrates and thoroughly analyzes the reduction of common battery cathode materials upon heating with NaCl-KCl under ambient air. Using the equimolar NMC and graphite as model material system resembling black mass, the reduction is shown to proceed via the halothermal and carbothermal stages. During the halothermal stage at 550−640 °C, lithium migrates from the host cathode particles into the chloride crystals via diffusion through graphite, leading to the decomposition of the initial structure into a mixture of transition metal oxides. The incorporation of lithium lowers the melting point of the chloride eutectic, and this effect is proportional to the relative amount of cathode material with respect to the salts. The molten chlorides coat the particles and graphite flakes, shielding them from the oxidative environment and enabling the carbothermal stage above 650 °C, during which the oxide phase gradually reduces to a metallic alloy.

The NMC622 cathode material undergoes a sequence of transformations similar to that of equimolar NMC, but the solid solution oxide converts to the metallic alloy by 720 °C. The NCA decomposes into a NiO-CoO mixture starting from 580 °C, and the Ni−Co alloy emerges at 620 °C, becoming the dominant phase by 700 °C. The LCO transforms into CoO from 530 °C, with nucleation of metallic Co beginning at 650 °C and completing by 740 °C. The LNMO gradually dissociates into $LiMnO_2$ and NiO-MnO between 450 and 520 °C, forming a complete solid solution of oxides at 530 °C, while the Ni−Mn alloy nucleates due to reduction of oxides above 630 °C. The LMO forms intermediate phases $LiMnO_2$ and Mn_3O_4 starting from 480 °C, and MnO appears above 540 °C, without further reduction to the metallic state. The LFP becomes a mixture of $Li_3Fe_2(PO_4)_3$ and Fe_2O_3 at 320−520 °C, but recrystallizes into the olivine structure above 530 °C.

The behavior of typical black-mass impurities in contact with the chloride salts is also investigated. The anode current collector material oxidizes in the 250−500 °C range, followed by gradual reduction to metallic Cu at higher temperatures. The cathode current collector remains as metallic Al until about 660 °C, after which it melts and may fuse with other metals. The PVDF binder melts at 180 °C and decomposes at 420 °C, while fluorine is captured by the chloride mixture. The LiF compound, a residue from battery electrolytes, remains stable until chloride melting, after which it dissolves in the melt.

The use of alkali chlorides not only enables the reduction to proceed without a protective gas atmosphere but also ensures effective separation of lithium from the transition metals. After dissolution of the heat-treated samples in water, up to 96% of Li is found in the recovered saline solution, while the insoluble fraction consists mostly of porous oxide particles and graphite. The proposed halometallurgical treatment could support the development of decentralized recycling infrastructure and promote a circular economy for battery materials.

■ ASSOCIATED CONTENT

Supporting Information

The Supporting Information is available free of charge at https://pubs.acs.org/doi/10.1021/acs.chemmater.5c02896.

It includes XRD patterns for starting materials (Figure S1), details of the in situ XRD experimental setup (Figure S2), and optical microscopy of NMC-Gr

https://doi.org/10.1021/acs.chemmater.5c02896
Chem. Mater. XXXX, XXX, XXX−XXX

together with SEM images of particle morphology after the heat treatment with NaCl-KCl (Figures S3, S4). The in situ XRD data are presented for NMC622-Gr with salts (Figure S5), equimolar NMC-Gr under nitrogen without salts (Figure S6), $LiPF_6$ and LFP-Gr (Figure S9), as well as Al/Cu impurities with Gr and NaCl-KCl (Figure S11). Additional characterization of chloride salts during cooling and after solidification is provided by in situ XRD and EDX (Figures S7, S8), together with ICP-OES results for insoluble and soluble fractions (Figure S10, Table S1). Finally, the relevance of halometallurgy for industrial black mass is demonstrated through XRD, DSC, and optical microscopy (Figures S12, S13, S14) (PDF)

AUTHOR INFORMATION

Corresponding Author

Arseniy Bokov − *Karlsruhe Institute of Technology (KIT), Institute for Applied Materials - Energy Storage Systems (IAM-ESS), Eggenstein-Leopoldshafen 76344, Germany; Helmholtz Institute Ulm for Electrochemical Energy Storage (HIU), Ulm 89081, Germany;* orcid.org/0000-0002-0293-8225; Email: arseniy.bokov@kit.edu

Authors

Anna Shelyug − *Karlsruhe Institute of Technology (KIT), Institute for Nuclear Waste Disposal (INE), Eggenstein-Leopoldshafen 76344, Germany;* orcid.org/0000-0003-3233-1632

Liuda Mereacre − *Karlsruhe Institute of Technology (KIT), Institute for Applied Materials - Energy Storage Systems (IAM-ESS), Eggenstein-Leopoldshafen 76344, Germany*

Michael Knapp − *Karlsruhe Institute of Technology (KIT), Institute for Applied Materials - Energy Storage Systems (IAM-ESS), Eggenstein-Leopoldshafen 76344, Germany;* orcid.org/0000-0003-0091-8463

Helmut Ehrenberg − *Karlsruhe Institute of Technology (KIT), Institute for Applied Materials - Energy Storage Systems (IAM-ESS), Eggenstein-Leopoldshafen 76344, Germany; Helmholtz Institute Ulm for Electrochemical Energy Storage (HIU), Ulm 89081, Germany;* orcid.org/0000-0002-5134-7130

Complete contact information is available at: https://pubs.acs.org/10.1021/acs.chemmater.5c02896

Notes

The authors declare no competing financial interest.

ACKNOWLEDGMENTS

This study was conducted as part of the research activities within CELEST (Center for Electrochemical Energy Storage Ulm-Karlsruhe). The authors are thankful to Michaela Nagel for assistance with optical microscopy and to Stephanie Kraft for ICP-OES measurements.

REFERENCES

(1) Maisel, F.; Neef, C.; Marscheider-Weidemann, F.; Nissen, N. F. A Forecast on Future Raw Material Demand and Recycling Potential of Lithium-Ion Batteries in Electric Vehicles. *Resour. Conserv. Recycl.* **2023**, *192*, 106920.

(2) Miao, Y.; Liu, L.; Zhang, Y.; Tan, Q.; Li, J. An Overview of Global Power Lithium-Ion Batteries and Associated Critical Metal Recycling. *J. Hazard. Mater.* **2022**, *425*, 127900.

(3) Dunn, J.; Slattery, M.; Kendall, A.; Ambrose, H.; Shen, S. Circularity of Lithium-Ion Battery Materials in Electric Vehicles. *Environ. Sci. Technol.* **2021**, *55* (8), 5189−5198.

(4) Gaines, L.; Richa, K.; Spangenberger, J. Key Issues for Li-Ion Battery Recycling. *MRS Energy Sustainability* **2018**, *5* (1), 12.

(5) Malik, M.; Chan, K. H.; Azimi, G. Review on the Synthesis of $LiNi_xMn_yCo_{1-x-y}O_2$ (NMC) Cathodes for Lithium-Ion Batteries. *Mater. Today Energy* **2022**, *28*, 101066.

(6) Purwanto, A.; Yudha, C. S.; Ubaidillah, U.; Widiyandari, H.; Ogi, T.; Haerudin, H. NCA Cathode Material: Synthesis Methods and Performance Enhancement Efforts. *Mater. Res. Express* **2018**, *5* (12), 122001.

(7) Liang, G.; Peterson, V. K.; See, K. W.; Guo, Z.; Pang, W. K. Developing High-Voltage Spinel $LiNi_{0.5}Mn_{1.5}O_4$ Cathodes for High-Energy-Density Lithium-Ion Batteries: Current Achievements and Future Prospects. *J. Mater. Chem. A* **2020**, *8* (31), 15373−15398.

(8) Lyu, Y.; Wu, X.; Wang, K.; Feng, Z.; Cheng, T.; Liu, Y.; Wang, M.; Chen, R.; Xu, L.; Zhou, J.; Lu, Y.; Guo, B. An Overview on the Advances of $LiCoO_2$ Cathodes for Lithium-Ion Batteries. *Adv. Energy Mater.* **2021**, *11* (2), 1−29.

(9) Bianchini, M.; Roca-Ayats, M.; Hartmann, P.; Brezesinski, T.; Janek, J. There and Back Again—The Journey of $LiNiO_2$ as a Cathode Active Material. *Angew. Chemie Int. Ed.* **2019**, *58* (31), 10434−10458.

(10) Huang, Y.; Dong, Y.; Li, S.; Lee, J.; Wang, C.; Zhu, Z.; Xue, W.; Li, Y.; Li, J. Lithium Manganese Spinel Cathodes for Lithium-Ion Batteries. *Adv. Energy Mater.* **2021**, *11* (2), 1−21.

(11) Bhar, M.; Ghosh, S.; Krishnamurthy, S.; Kaliprasad, Y.; Martha, S. K. A Review on Spent Lithium-Ion Battery Recycling: From Collection to Black Mass Recovery. *RSC Sustainability* **2023**, *1* (5), 1150−1167.

(12) Donnelly, L.; Pirrie, D.; Power, M.; Corfe, I.; Kuva, J.; Lukkari, S.; Lahaye, Y.; Liu, X.; Dehaine, Q.; Jolis, E. M.; Butcher, A. The Recycling of End-of-Life Lithium-Ion Batteries and the Phase Characterisation of Black Mass. *Recycling* **2023**, *8* (4), 59.

(13) Vanderbruggen, A.; Gugala, E.; Blannin, R.; Bachmann, K.; Serna-Guerrero, R.; Rudolph, M. Automated Mineralogy as a Novel Approach for the Compositional and Textural Characterization of Spent Lithium-Ion Batteries. *Miner. Eng.* **2021**, *169*, 106924.

(14) Jung, J. C.-Y.; Sui, P.-C.; Zhang, J. A Review of Recycling Spent Lithium-Ion Battery Cathode Materials Using Hydrometallurgical Treatments. *J. Energy Storage* **2021**, *35*, 102217.

(15) Makuza, B.; Tian, Q.; Guo, X.; Chattopadhyay, K.; Yu, D. Pyrometallurgical Options for Recycling Spent Lithium-Ion Batteries: A Comprehensive Review. *J. Power Sources* **2021**, *491*, 229622.

(16) Neumann, J.; Petranikova, M.; Meeus, M.; Gamarra, J. D.; Younesi, R.; Winter, M.; Nowak, S. Recycling of Lithium-Ion Batteries—Current State of the Art, Circular Economy, and Next Generation Recycling. *Adv. Energy Mater.* **2022**, *12* (17), 2102917.

(17) Liang, Z.; Cai, C.; Peng, G.; Hu, J.; Hou, H.; Liu, B.; Liang, S.; Xiao, K.; Yuan, S.; Yang, J. Hydrometallurgical Recovery of Spent Lithium Ion Batteries: Environmental Strategies and Sustainability Evaluation. *ACS Sustainable Chem. Eng.* **2021**, *9* (17), 5750−5767.

(18) Davis, K.; Demopoulos, G. P. Hydrometallurgical Recycling Technologies for NMC Li-Ion Battery Cathodes: Current Industrial Practice and New R&D Trends. *RSC Sustainable* **2023**, *1* (8), 1932−1951.

(19) Lombardo, G.; Ebin, B.; Foreman, M. R. S. J.; Petranikova, B.-M.; Petranikova, M. Chemical Transformations in Li-Ion Battery Electrode Materials by Carbothermic Reduction. *ACS Sustainable Chem. Eng.* **2019**, *7* (16), 13668−13679.

(20) Fu, Y.; He, Y.; Li, J.; Qu, L.; Yang, Y.; Guo, X.; Xie, W. Improved Hydrometallurgical Extraction of Valuable Metals from Spent Lithium-Ion Batteries via a Closed-Loop Process. *J. Alloys Compd.* **2020**, *847*, 156489.

(21) Zhu, X.; Li, Y.; Gong, M.; Mo, R.; Luo, S.; Yan, X.; Yang, S. Recycling Valuable Metals from Spent Lithium-Ion Batteries Using

Carbothermal Shock Method. *Angew. Chem.* **2023**, *135* (15), No. e202300074.
(22) Zhang, J.; Liang, G.; Yang, C.; Hu, J.; Chen, Y.; Wang, C. A Breakthrough Method for the Recycling of Spent Lithium-Ion Batteries without Pre-Sorting. *Green Chem.* **2021**, *23* (21), 8434−8440.
(23) Stallmeister, C.; Friedrich, B. Influence of Flow-Gas Composition on Reaction Products of Thermally Treated NMC Battery Black Mass. *Metals* **2023**, *13* (5), 923.
(24) Stallmeister, C.; Friedrich, B. Holistic Investigation of the Inert Thermal Treatment of Industrially Shredded NMC 622 Lithium-Ion Batteries and Its Influence on Selective Lithium Recovery by Water Leaching. *Metals* **2023**, *13* (12), 2000.
(25) Lombardo, G.; Ebin, B.; Steenari, B.-M.; Alemrajabi, M.; Karlsson, I.; Petranikova, M. Comparison of the Effects of Incineration, Vacuum Pyrolysis and Dynamic Pyrolysis on the Composition of NMC-Lithium Battery Cathode-Material Production Scraps and Separation of the Current Collector. *Resour. Conserv. Recycl.* **2021**, *164*, 105142.
(26) Dash, A.; Vaßen, R.; Guillon, O.; Gonzalez-Julian, J. Molten Salt Shielded Synthesis of Oxidation Prone Materials in Air. *Nat. Mater.* **2019**, *18* (5), 465−470.
(27) Dash, A.; Sohn, Y. J.; Vaßen, R.; Guillon, O.; Gonzalez-Julian, J. Synthesis of Ti_3SiC_2 MAX Phase Powder by a Molten Salt Shielded Synthesis (MS^3) Method in Air. *J. Eur. Ceram. Soc.* **2019**, *39* (13), 3651−3659.
(28) Roy, C.; Banerjee, P.; Bhattacharyya, S. Molten Salt Shielded Synthesis (MS3) of Ti_2AlN and V_2AlC MAX Phase Powders in Open Air. *J. Eur. Ceram. Soc.* **2020**, *40* (3), 923−929.
(29) Vanderbruggen, A.; Hayagan, N.; Bachmann, K.; Ferreira, A.; Werner, D.; Horn, D.; Peuker, U.; Serna-Guerrero, R.; Rudolph, M. Lithium-Ion Battery Recycling—Influence of Recycling Processes on Component Liberation and Flotation Separation Efficiency. *ACS EST Eng.* **2022**, *2* (11), 2130−2141.
(30) Babanejad, S.; Ahmed, H.; Andersson, C.; Samuelsson, C.; Lennartsson, A.; Hall, B.; Arnerlöf, L. High-Temperature Behavior of Spent Li-Ion Battery Black Mass in Inert Atmosphere. *J. Sustainable Metall.* **2022**, *8* (1), 566−581.
(31) Wei, X.; Guo, Z.; Zhao, Y.; Sun, Y.; Hankin, A.; Titirici, M. Recovery of Graphite from Industrial Lithium-Ion Battery Black Mass. *RSC Sustainable* **2025**, *3* (1), 264−274.
(32) Zanoletti, A.; Cornelio, A.; Borgese, L.; Siviero, G.; Cinosi, A.; Galli, E.; Bontempi, E. Sample Preparation Procedures for Elemental Analysis of Critical Raw Materials in Lithium-Ion Battery Black Mass: Challenges Responding to the Supplementary Battery Recycling Regulation. *J. Environ. Manage.* **2025**, *380*, 124973.
(33) Sergeev, D.; Kobertz, D.; Müller, M. Thermodynamics of the NaCl−KCl System. *Thermochim. Acta* **2015**, *606*, 25−33.
(34) Anwar, J.; Leitold, C.; Peters, B. Solid−solid Phase Equilibria in the NaCl−KCl System. *J. Chem. Phys.* **2020**, *152* (14), 144109.
(35) Pritzl, D.; Teufl, T.; Freiberg, A. T. S.; Strehle, B.; Sicklinger, J.; Sommer, H.; Hartmann, P.; Gasteiger, H. A. Washing of Nickel-Rich Cathode Materials for Lithium-Ion Batteries: Towards a Mechanistic Understanding. *J. Electrochem. Soc.* **2019**, *166* (16), A4056−A4066.
(36) Chen, H.; Mattsson, A.-M.; King, L.; Liu, H.; Nielsen, I.; Ericson, T.; Preobrajenski, A.; Brant, W. R.; Hahlin, M. Study of Degradation Mechanisms in Aqueous-Processed Ni-Rich Cathodes for Enhanced Sustainability of Batteries. *J. Mater. Chem. A* **2024**, *12* (37), 25393−25406.
(37) Sasaki, S.; Fujino, K.; Takeuchi, Y. X-Ray Determination of Electron-Density Distributions in Oxides, MgO, MnO, CoO, and NiO, and Atomic Scattering Factors of Their Constituent Atoms. *Proc. Jpn. Acad., Ser. B* **1979**, *55* (2), 43−48.
(38) Zheng, Y.; Shao, P.; Yang, L.; Huang, Y.; Zhang, H.; Fang, L.; Qiu, C.; Tang, H.; Shao, J.; Luo, X. Gas Exchange-Driven Carbothermal Reduction for Simultaneous Lithium Extraction from Anode and Cathode Scraps. *Resour. Conserv. Recycl.* **2023**, *188*, 106696.
(39) Yan, Z.; Sattar, A.; Li, Z. Priority Lithium Recovery from Spent Li-Ion Batteries via Carbothermal Reduction with Water Leaching. *Resour. Conserv. Recycl.* **2023**, *192*, 106937.
(40) Konar, S.; Häusserman, U.; Svensson, G. Intercalation Compounds from LiH and Graphite: Relative Stability of Metastable Stages and Thermodynamic Stability of Dilute Stage I D. *Chem. Mater.* **2015**, *27* (7), 2566−2575.
(41) Oka, H.; Makimura, Y.; Uyama, T.; Nonaka, T.; Kondo, Y.; Okuda, C. Changes in the Stage Structure of Li-Intercalated Graphite Electrode at Elevated Temperatures. *J. Power Sources* **2021**, *482*, 228926.
(42) Nixon, D. E.; Parry, G. S. Formation and Structure of the Potassium Graphites. *J. Phys. D.: Appl. Phys.* **1968**, *1* (3), 303.
(43) Nishitani, R.; Uno, Y.; Suematsu, H. In Situ Observation of Staging in Potassium-Graphite Intercalation Compounds. *Phys. Rev. B* **1983**, *27* (10), 6572−6575.
(44) Song, T.; Xie, Y.; Chen, Y.; Guo, H. Thermodynamics of Graphite Intercalation Binary Alloys of Li-Na, Na-K, and Li-K from van Der Waals Density Functionals. *J. Solid State Electrochem.* **2019**, *23* (10), 2825−2834.
(45) Sangster, J.; Pelton, A. D. Phase Diagrams and Thermodynamic Properties of the 70 Binary Alkali Halide Systems Having Common Ions. *J. Phys. Chem. Ref. Data* **1987**, *16* (3), 509−561.
(46) Hao, L.; Sridar, S.; Xiong, W. Thermodynamic Description of Molten Salt Systems: KCl-LiCl-NaCl and KCl-LiCl-$NdCl_3$. *J. Mol. Liq.* **2023**, *382* (April), 121869.
(47) Hérold, C.; Hérold, A.; Lagrange, P. New Synthesis Routes for Donor-Type Graphite Intercalation Compounds. *J. Phys. Chem. Solids* **1996**, *57* (6−8), 655−662.
(48) Janiak, C.; Hoffmann, R.; Sjovall, P.; Kasemo, B. The Potassium Promoter Function in the Oxidation of Graphite: An Experimental and Theoretical Study. *Langmuir* **1993**, *9* (12), 3427−3440.
(49) Duemmler, K.; Lin, Y.; Woods, M.; Karlsson, T.; Gakhar, R.; Beeler, B. Evaluation of Thermophysical Properties of the LiCl-KCl System via Ab Initio and Experimental Methods. *J. Nucl. Mater.* **2022**, *559*, 153414.
(50) Ding, W.; Gong, Q.; Liang, S.; Hoffmann, R.; Zhou, H.; Li, H.; Wang, K.; Zhang, T.; Weisenburger, A.; Müller, G.; et al. Multi-Cationic Molten Salt Electrolyte of High-Performance Sodium Liquid Metal Battery for Grid Storage. *J. Power Sources* **2023**, *553*, 232254.
(51) Joncourt, L.; Mermoux, M.; Touzain, P.; Bonnetain, L.; Dumas, D.; Allard, B. Sodium Reactivity with Carbons. *J. Phys. Chem. Solids* **1996**, *57* (6−8), 877−882.
(52) Moriwake, H.; Kuwabara, A.; Fisher, C. A. J.; Ikuhara, Y. Why Is Sodium-Intercalated Graphite Unstable? *RSC Adv.* **2017**, *7* (58), 36550−36554.
(53) Lonergan, J.; Goncharov, V.; Swinhart, M.; Makovsky, K.; Rollog, M.; McNamara, B.; Clark, R.; Cutforth, D.; Armstrong, C.; Guo, X.; Paviet, P. Thermodynamic Investigation of the NaCl-KCl Salt System from 25 to 950 °C. *J. Mol. Liq.* **2023**, *391* (PA), 122591.
(54) Fancher, D. L.; Barsch, G. R. Lattice Theory of Alkali Halide Solid Solutions-II. Entropy of Mixing and Solid Solubility. *J. Phys. Chem. Solids* **1969**, *30* (11), 2517−2525.
(55) Fancher, D. L.; Barsch, G. R. Lattice Theory of Alkali Halide Solid Solutions-I. Heat of Formation. *J. Phys. Chem. Solids* **1969**, *30* (11), 2503−2516.
(56) Velázquez-Martínez, O.; Valio, J.; Santasalo-Aarnio, A.; Reuter, M.; Serna-Guerrero, R. A Critical Review of Lithium-Ion Battery Recycling Processes from a Circular Economy Perspective. *Batteries* **2019**, *5* (4), 68.
(57) Juzeliūnas, E.; Fray, D. J. Silicon Electrochemistry in Molten Salts. *Chem. Rev.* **2020**, *120* (3), 1690−1709.
(58) Wang, M.; Liu, K.; Yu, J.; Zhang, Q.; Zhang, Y.; Valix, M.; Tsang, D. C. W. Challenges in Recycling Spent Lithium-Ion Batteries: Spotlight on Polyvinylidene Fluoride Removal. *Global Challenges* **2023**, *7* (3), 2200237.
(59) Porvali, A.; Mäkelä, T.; Bachér, J. Observations on the Leaching of Milled Black Mass with Additives. *J. Sustainable Metall.* **2023**, *9* (2), 816−825.

https://doi.org/10.1021/acs.chemmater.5c02896
Chem. Mater. XXXX, XXX, XXX−XXX

(60) Qu, X.; Zhang, B.; Zhao, J.; Qiu, B.; Chen, X.; Zhou, F.; Li, X.; Gao, S.; Wang, D.; Yin, H. Salt-Thermal Methods for Recycling and Regenerating Spent Lithium-Ion Batteries: A Review. *Green Chem.* **2023**, *25* (8), 2992−3015.
(61) Liu, Y.; Zhang, X.; Ma, W.; Duan, H.; Zhao, Q.; Liang, Z. A Comprehensive Review of the Recovery of Spent Lithium-Ion Batteries with Molten Salt Method: Progress, Shortcomings and Prospects. *J. Energy Storage* **2024**, *99* (PB), 113407.
(62) Murphy, O.; Haji, M. N. A Review of Technologies for Direct Lithium Extraction from Low Li^+ Concentration Aqueous Solutions. *Front. Chem. Eng.* **2022**, *4*, 1008680.
(63) Baudino, L.; Santos, C.; Pirri, C. F.; La Mantia, F.; Lamberti, A. Recent Advances in the Lithium Recovery from Water Resources: From Passive to Electrochemical Methods. *Adv. Sci.* **2022**, *9* (27), 2201380.
(64) Farahbakhsh, J.; Arshadi, F.; Mofidi, Z.; Mohseni-Dargah, M.; Kök, C.; Assefi, M.; Soozanipour, A.; Zargar, M.; Asadnia, M.; Boroumand, Y.; et al. Direct Lithium Extraction: A New Paradigm for Lithium Production and Resource Utilization. *Desalination* **2024**, *575*, 117249.
(65) Li, M.; Mo, R.; Ding, A.; Zhang, K.; Guo, F.; Xiao, C. Electrochemical Technology to Drive Spent Lithium-Ion Batteries (LIBs) Recycling: Recent Progress, and Prospects. *Energy Mater.* **2024**, *4*, 400070.
(66) Vanderbruggen, A.; Salces, A.; Ferreira, A.; Rudolph, M.; Serna-Guerrero, R. Improving Separation Efficiency in End-of-Life Lithium-Ion Batteries Flotation Using Attrition Pre-Treatment. *Minerals* **2022**, *12* (1), 72.
(67) Tahmasebi, M. H.; Obrovac, M. N. New Insights into the All-Dry Synthesis of NMC622 Cathodes Using a Single-Phase Rock Salt Oxide Precursor. *ACS Omega* **2024**, *9* (1), 1916−1924.
(68) Zhang, N.; Xu, Z.; Deng, W.; Wang, X. Recycling and Upcycling Spent LIB Cathodes: A Comprehensive Review. *Electrochem. Energy Rev.* **2022**, *5* (S1), 33.
(69) Langdon, J.; Manthiram, A. A Perspective on Single-Crystal Layered Oxide Cathodes for Lithium-Ion Batteries. *Energy Storage Mater.* **2021**, *37*, 143−160.
(70) Huang, M.; Wang, M.; Yang, L.; Wang, Z.; Yu, H.; Chen, K.; Han, F.; Chen, L.; Xu, C.; Wang, L.; Shao, P.; Luo, X. Direct Regeneration of Spent Lithium-Ion Battery Cathodes: From Theoretical Study to Production Practice. *Nano-Micro Lett.* **2024**, *16* (1), 207.

https://doi.org/10.1021/acs.chemmater.5c02896
Chem. Mater. XXXX, XXX, XXX−XXX